

# Resonant Enhancement of Exchange Coupling for Voltage-Controlled Magnetic Switching


Shehrin Sayed<sup>1,2,\*</sup>, Cheng-Hsiang Hsu<sup>1</sup>, Niklas Roschewsky,<sup>3</sup> See-Hun Yang<sup>4</sup>, and Sayeef Salahuddin<sup>1,2,†</sup>

<sup>1</sup>*Electrical Engineering and Computer Sciences, University of California, Berkeley, California 94720, USA*

<sup>2</sup>*Materials Sciences Division, Lawrence Berkeley National Laboratory, Berkeley, California 94720, USA*

<sup>3</sup>*Department of Physics, University of California, Berkeley, California 94720, USA*

<sup>4</sup>*IBM Research – Almaden, San Jose, California 95120, USA*

 (Received 18 April 2020; revised 19 July 2020; accepted 3 September 2020; published 30 September 2020)

We predict that it is possible to achieve a purely voltage-driven switching of a ferromagnet using spin-dependent resonant tunneling. In a configuration of two exchange-coupled magnets through a resonant-tunneling barrier, application of a voltage leads to a resonant enhancement and an oscillatory nature of the exchange coupling. The peak equivalent exchange field is strong enough to switch typical ferromagnets used in scaled magnetic memory devices. The switched configuration is retained once the electric field is removed since the equilibrium exchange coupling is negligible, suppressed by large barriers. Bidirectional switching is possible with the same polarity of the voltage, unlike conventional magnetic memory devices where a bidirectional current or a magnetic field is necessary. Further, the threshold of switching is decoupled from the speed, due to the conservative nature of the exerted torque. This is very different from the conventional spin-torque devices that exhibit a trade-off due to the non-conservative nature of the switching torque. We further show that the structure shows an oscillation in the magnetoresistance (MR) stemming from the resonant tunneling. Interestingly, the MR is higher for smaller voltages while the exchange field is higher for larger voltages—this is promising for efficient read and write operations in potential memory applications.

DOI: [10.1103/PhysRevApplied.14.034070](https://doi.org/10.1103/PhysRevApplied.14.034070)

## I. INTRODUCTION

Magnetization switching using current-induced spin-transfer torque (STT) [1,2] and spin-orbit torque (SOT) [3–5] has attracted increasing interest for nonvolatile memory technologies like magnetoresistive random-access memory (MRAM) [6–9]. However, the large switching current density is a limiting factor to the technological advancement in terms of the energy efficiency and bit density. Recently, there is a growing interest in the voltage or electric-field-controlled switching mechanisms [10–14] as a possible solution to issues involving memory bandwidth and high-power consumption [12,15].

In this paper, we propose a two-terminal structure, which can control the interlayer exchange coupling (IEC) between the fixed and the free magnets using an electric field. The magnets are separated by two tunnel barriers sandwiching a thin layer of a nonmagnetic spacer [see Fig. 1(a)]. The electric field control of IEC is achieved via the resonant tunneling phenomena due to a quantum-well

(QW) formation within the spacer layer. We use nonequilibrium Green's function (NEGF) based quantum-transport simulations to show that a voltage-dependent IEC can be induced using existing materials [see Fig. 1(b)]. The sign of the induced IEC energy changes periodically with a growing magnitude as a function of the applied voltage.

The voltage-induced positive and negative IEC energy can switch the free magnet to have either an antiferromagnetic (AFM) or a ferromagnetic (FM) configuration with respect to the fixed magnet, if the IEC magnitude is greater than a threshold value determined by the anisotropy energies of the magnets. This indicates that a bidirectional switching is possible for the same voltage polarity, which is quite different from the existing mechanisms. The configuration after the switching is retained once the electric field is removed because the tunnel barriers suppress the IEC at equilibrium.

We further show that the IEC-assisted switching threshold is independent of the Gilbert damping and the demagnetizing field, which is a manifestation of the conservative nature of the exerted torque. This means that switching voltage and speed of switching can be independently optimized by engineering the magnetic anisotropy and the

\*ssayed@berkeley.edu

†sayeef@berkeley.edu

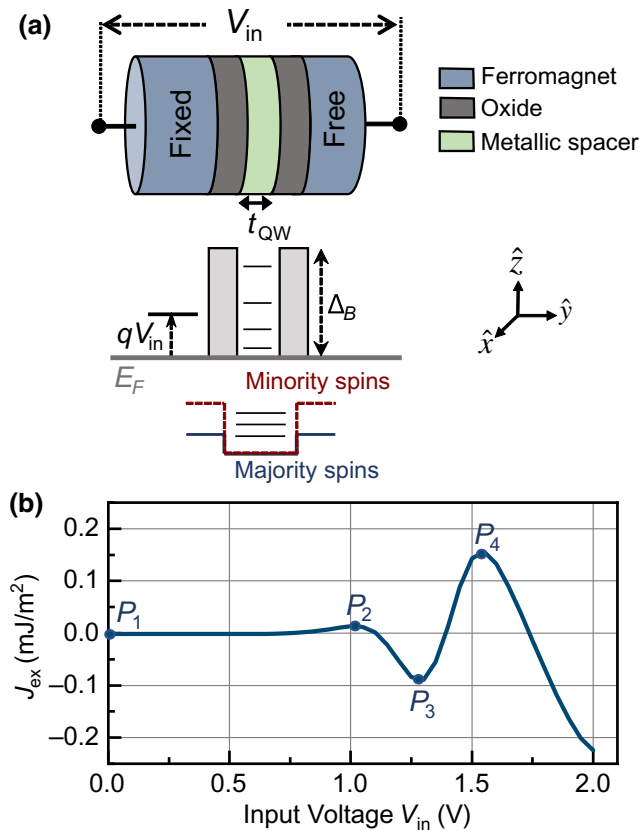


FIG. 1. (a) The proposed composite magnetic-tunnel-junction structure with two oxide barriers sandwiching a metallic spacer. The two barriers form a quantum well with discrete states within the metallic spacer. The structure can control the transmission coefficient between the two magnets via resonant tunneling, which results in a control on the IEC energy. (b) The bias-dependent IEC changes sign in a periodic manner and grows in magnitude for higher electric field. For simulation, barrier heights are 0.7 eV and widths are 1 nm each. The spacer thickness is 0.8 nm.

Gilbert damping, respectively. This is qualitatively different from the conventional spin-torque devices, which exhibit a trade-off between these two parameters due to the nonconservative nature of the exerted torque.

Similar voltage control of IEC over a single tunnel barrier has been discussed in the past using high voltage tunneling [16], mobile oxygen vacancies within oxides [11], and temperature-driven insulator-to-metal transition [17]. However, sufficiently strong IEC energy as needed for practical functionalities could be limited by the oxide breakdown, long switching time due to the slow migration of the oxygen ions [18,19], and wide operating temperature requirements, respectively. An electric-field-driven but volatile transition from AFM-to-FM configuration and vice versa in a spin valve has been discussed using an ionic liquid gating [20]. Recently, a similar control of

exchange coupling has been discussed using an oxide gate for electric field induced switching [21].

Here, we utilize the resonant-tunneling phenomena to induce a substantial IEC that can enable magnetization switching in a nonvolatile manner. We argue that the resonant tunneling and the induced IEC strength together can be optimized by various material choices and device structures to lower the operating voltage and current. These unique features of the proposed structure is promising for devices with substantially improved energy-delay product.

We expect a voltage-dependent oscillation in the magnetoresistance of the structure, similar to those observed in the past [22–26] due to the resonant tunneling. Interestingly, the MR decreases as a function of the voltage; yet the strength of the IEC increases. Large MR below switching threshold enables efficient read operation.

The paper is organized as follows. In Sec. II, we discuss the mechanism for electric field control of IEC in the proposed structure. In Sec. III, we discuss the IEC-induced magnetization dynamics. We present models for the threshold and the speed of the IEC-induced switching and compare with the conventional mechanisms. In Sec. IV, we provide results and discussion on how the device can be optimized to lower the operating current and voltage in the structure. We end with a brief summary in Sec. V.

## II. ELECTRIC FIELD CONTROL OF THE INTERLAYER EXCHANGE COUPLING

### A. Basic mechanism

It is well established that two FMs separated by a thin metallic [27–30] or a nonmetallic [24,31] spacer have an equilibrium configuration (FM or AFM) dictated by the IEC. The IEC originates due to a quantum interference of spin-dependent wave functions, as the majority and the minority spins see different barriers at the magnetic interfaces leading to different spin-dependent QWs below the equilibrium Fermi level ( $E_F$ ) [32–35]. The IEC energy periodically changes sign as a function of the spacer thickness, which has been observed experimentally as a periodic change in the magnetic configuration between AFM and FM [24,27–31]. Such spin-dependent interference at the magnetic interfaces is significantly reduced in the presence of a thick oxide barrier [36,37], and the two FMs do not have a preferential configuration at equilibrium.

We introduce two oxide barriers at the two magnetic interfaces [see Fig. 1(a)] to suppress the equilibrium IEC. We insert a thin metallic spacer between the two oxide barriers, which form a QW within the metallic spacer with discrete energy states above  $E_F$ . At equilibrium, the contact electrochemical potentials are at the  $E_F$ . We can apply an electric field across the structure to tune the contact electrochemical potential to one of these discrete states. At these discrete states, the transmission coefficients across the structure becomes very high, as typically seen for the

widely used resonant-tunneling diodes [38]. Subsequently, the two FMs feel a substantial IEC as the spin-dependent wave functions can travel through the metallic spacer and interfere. The spin-dependent interference can be constructive or destructive, depending on the transmission coefficient of the structure. The electric field control of the transmission coefficient induces an IEC ( $J_{\text{ex}}$ ), which alternates sign as a function of the voltage [see Fig. 1(b)]. The resonant-tunneling-induced IEC is robust to incoherent scattering with momentum and phase-relaxation processes, which are discussed later. The strength of the IEC increases with the number of occupied states. For brevity we call the structure shown in Fig. 1(a) resonant-exchange-controlled MRAM (REC MRAM).

Resonant tunneling within a magnetic structure has been demonstrated up to room temperature in a double-barrier magnetic tunnel junction (MTJ) [22,23,39], where the QW forms within a relatively thicker magnetic spacer layer. They report a voltage-dependent oscillation in the magnetoresistance due to a spin-selective tunneling phenomena. Here, we discuss a spin-dependent resonant tunneling where the QW is formed within a thin nonmagnetic spacer layer, specifically a material that is known to exhibit large equilibrium IEC in the absence of the tunnel barriers. Resonant tunneling through such a nonmagnetic spacer will exploit the property of the material and will exhibit a bias-dependent oscillation in IEC.

### B. Model

The bilinear IEC energy density between the two magnets is given by [32–34]

$$J_{\text{ex}} = \Delta E_{\text{FM}} - \Delta E_{\text{AFM}}, \quad (1)$$

where  $\Delta E = \int_{-\infty}^{+\infty} E \Delta n_s dE$  [32] is the energy-density change across the QW due to an imbalance of the spin density  $\Delta n_s = n_s(d) - n_s(0)$  caused by the quantum interference. The subscripts FM and AFM refer to ferromagnetic and antiferromagnetic, respectively.

We analyze the structure with NEGF-based calculations using a single-band effective-mass tight-binding Hamiltonian. We assume that the structure under consideration is spatially uniform along the transverse directions and transverse modes are nearly decoupled so that transport can be analyzed with a one-dimensional (1D) Hamiltonian for every mode. The spin density in the structure is given by

$$n_s = \frac{1}{2\pi} \int D_0 \text{Re} [\text{Tr} (\sigma_z G^n)] d\epsilon_T, \quad (2)$$

where  $\epsilon_T = \hbar^2 (k_y^2 + k_z^2)/2m^*$  is the energy along the transverse plane  $y$ - $z$ ,  $D_0$  is the two-dimensional (2D) density of states on the transverse plane,  $\sigma_z$  is the  $z$ -Pauli matrix, and  $G^n$  is the correlation function. We approximate

the  $D_0$  with the 2D density of states of the bulk given by  $m^*/\pi \hbar^2$  where  $m^*$  is the effective mass and  $\hbar = h/2\pi$ .

The correlation function is obtained as

$$G^n = \sum_j f_j A_j, \quad (3)$$

where  $f_j = 1/\{1 + \exp[(E - \mu_j)/k_B T]\}$  is the occupation factor of  $j$ th contact with contact electrochemical potential  $\mu_j$ ,  $E$  is the energy,  $A_j = G^R \Gamma_j (G^R)^\dagger$  is the spectral function with  $\Gamma_j$  being the broadening function of the  $j$ th contact,  $G^R = [EI - H - \Sigma]^{-1}$  is Green's function,  $\Sigma$  is the total self-energy of the contacts, and  $H$  is the Hamiltonian of the structure. We assume that the voltage applied across the two-terminal structure mostly drops across the two oxide barriers. Details of the NEGF-based calculations are given in Appendix A.

In principle, a biquadratic component of exchange coupling can coexist [40], which do not change sign [32]. Such a component is included in our Hamiltonian and can be calculated using the NEGF formalism presented here. However, in this paper, we specifically focus on the voltage control of the bilinear IEC component. This is because the bilinear component with a particular sign is well known for altering the system energy such that the magnetizations switch to become either parallel or antiparallel to satisfy the minimum energy condition, even when the magnets are perfectly aligned [32–34]. Such a strong effect of the bilinear component has been well studied in equilibrium, within structures consisting of Co/Fe-based magnets and transition metal spacers [24,27–31].

### C. Materials and structure

A choice for the spacer layer could be the transition metals, e.g., Rh, Ru, Ir, Re, and Cu [27,41,42], which are well known for exhibiting large IEC at equilibrium and widely used in synthetic antiferromagnets. The strength of the IEC across such a metallic spacer depends on the shape of the spin-dependent QW formed below  $E_F$ , which is largely determined by the mismatch between the  $d$ -electron bands of the FM and the metallic spacer [27,35], growth condition, and hybridization at the interfaces [42]. Oxides like NiO could be a choice as well since it exhibit large oscillatory IEC at equilibrium [24]. The parameters used to simulate the structure in Fig. 1(a) are calibrated using several room-temperature experiments, as described below. The parameters are listed as Table I in Appendix A.

We fix the parameters for the spacer and the FM layers by simulating a FM|spacer|FM structure [see, Fig. 2(a)] and comparing with the equilibrium experiments on similar structures that exhibit a periodic oscillation in IEC as a function of the spacer thickness ( $d$ ). The simulation shows the expected oscillatory nature of the equilibrium IEC due to the spin-dependent quantum interference [32–34],

which behaves like a decaying sinusoidal function. This oscillatory IEC has been observed in various experiments [24,27–31]. Our model parameters are such that the calculated equilibrium IEC energy [solid line in Fig. 2(a)] corresponds to the experimental observations in a Co|Ru|Co system [27] [scatter points in Fig. 2(a)], i.e., the first AFM IEC strength is around approximately 5 mJ/m<sup>2</sup> occurring around approximately 6 Å and the IEC oscillation period is  $\lambda_{\text{IEC}} \approx 11$  Å. The periodicity of the equilibrium IEC is related to the depth of the spin-dependent QW ( $\Delta_{\text{sp}}$ ) as

$$\lambda_{\text{IEC}} = \frac{h}{2\sqrt{2m^* \Delta_{\text{sp}}}}, \quad (4)$$

in agreement with the NEGF simulation [see Fig. 2(b)].

The oxide parameters are calibrated with experiments on FM|MgO|FM structures. First, we calibrate with the equilibrium IEC as a function of the oxide thickness  $d$  [see Fig. 2(c)]. Our simulation shows a sizable IEC for thin oxides (below approximately 5 Å) due to the tunneling effect, that drastically decreases for thicker oxides [solid line in Fig. 2(c)]. A similar trend has been experimentally observed in MgO-based structures [36,37] [scatter points

Fig. 2(c)]. Note that the experiments observe a sizable IEC up to approximately 8 Å, possibly due to defects and pinholes in the MgO. Such a trend can be reproduced in our simulations using a lower barrier height. We use a barrier height  $\Delta_B = 0.7$  eV as typically expected in MgO [43,44]. We further calibrate the parameters, by comparing the simulation results on bias-dependent fieldlike [ $\propto \vec{J}_s \cdot (\vec{m}_1 \times \vec{m}_2)$ ] and dampinglike [ $\propto \vec{J}_s \cdot (\vec{m}_1 \times \vec{m}_1 \times \vec{m}_2)$ ] spin-transfer torques [solid lines in Fig. 2(d)] with experimental observations [39] in MgO-based magnetic tunnel junctions [scatter points in Fig. 2(d)]. NEGF results reproduce the experimentally observed bias-dependent asymmetry in the dampinglike torque and the quadratic dependence for the fieldlike torque, as previously discussed in Ref. [46].

For the structure in Fig. 1(a), we set the spacer thickness to 0.8 nm and the oxide barrier thickness to 1 nm each. The barrier heights are set around 0.7 eV, as typically observed for MgO [43,44]. Thus, assuming simulation parameters equivalent to a Co-based alloy(10 nm)—MgO(1 nm)—Ru(0.8 nm)—MgO(1 nm)—Co-based alloy(1.5 nm) structure, we expect the structure to induce a resonant enhancement in the IEC energy as large as 0.2 mJ/m<sup>2</sup>,

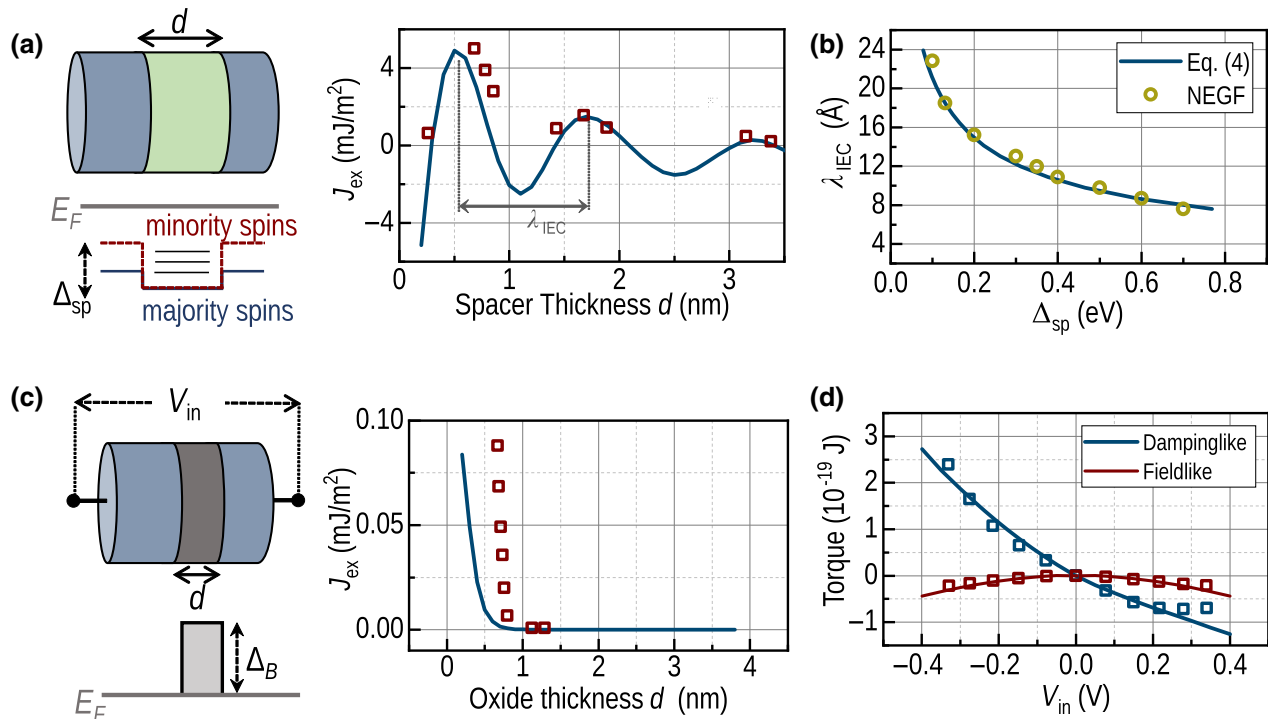


FIG. 2. Materials parameter calibration. (a) NEGF simulation of the oscillatory equilibrium IEC (solid lines) as a function of metallic spacer thickness  $d$ . The parameters are such that the simulation agrees with experiments on a Co|Ru|Co system [27] (scatter points). The first peak occurs at approximately 6 Å with IEC approximately 5 mJ/m<sup>2</sup> and a periodicity  $\lambda_{\text{IEC}} \approx 11$  Å. (b) The periodicity of equilibrium IEC ( $\lambda_{\text{IEC}}$ ) depends on the spin-dependent quantum well (with a depth  $\Delta_{\text{sp}}$ ) formed below the Fermi level due to a  $d$ -orbital mismatch between the FM and the spacer. NEGF simulation (solid line) of (c) the equilibrium IEC across an oxide spacer. Thin oxide ( $< 5$  Å) exhibits a large IEC due to tunneling effect, which drastically reduces for thick oxides, similar to the experimental observations across MgO in Refs. [43,44] (scatter points). (d) Bias-dependent nature of the dampinglike and fieldlike torques on the free layer in MgO-based MTJs, compared with the experiments (scatter points) in Ref. [45].



within an applied voltage range of 0 to 2 V. Here, 2 V corresponds to an electric field of approximately 10 MV/cm. The equilibrium IEC (at 0 V) is negligible (approximately  $10^{-6}$  mJ/m<sup>2</sup>). Note that the oscillation observed in the resonance-enhanced IEC is sinusoidal in nature, similar to the oscillation observed in the equilibrium case [in Fig. 2(a)]. This is because the resonance-enhanced IEC also arises due to the quantum interference of the spin-dependent wave functions and its voltage periodicity is related to the equilibrium periodicity  $\lambda_{\text{IEC}}$ , which is discussed later.

In a memory array, the operating temperature could be higher due to heating and the device performance can change. The operation of the proposed device depends on two key phenomena: the resonant tunneling and the inter-layer exchange coupling. The resonant tunneling is not significantly affected by such temperature variations [47], but IEC energy may vary upon heating. It has been discussed in the past that an increase in temperature is expected to decrease IEC across a metallic spacer, but increases IEC across an oxide spacer [33]. However, the decrease in IEC across a thin metallic spacer is not significant up to 400 K (see, e.g., Ref. [48,49]). In the proposed device, the spacer is a composite of both metal and oxide, and a temperature-dependent analysis of the device performance we leave as future work.

### III. IEC-ASSISTED MAGNETIZATION DYNAMICS

#### A. Magnetization switching

The resonance-enhanced IEC shown in Fig. 1(b) will switch the free magnet to have either FM or AFM configurations with respect to the fixed magnet, determined by the IEC sign. In this paper, positive and negative IEC indicates AFM and FM configurations, respectively. The configuration after switching will be retained once the electric field is removed because the equilibrium IEC is negligible due to the presence of the thick oxide barriers. We simulate the magnetization dynamics with a voltage pulse applied across the structure. The magnetization dynamics are simulated with an exchange-coupled Landau-Lifshitz-Gilbert (LLG) model [50,51] assuming single-domain magnets, in conjunction with the NEGF formalism. We apply three consecutive voltage pulses as shown in Fig. 3(a), with the pulse width being 5 ns each and pulse heights corresponding to  $P_4$ ,  $P_3$ , and  $P_2$  points in Fig. 1(b), respectively. Corresponding time-dependent dynamics of the  $z$ ,  $x$ , and  $y$  components of the magnetization are shown in Figs. 3(b)–3(d), respectively.

We start with a ferromagnetic configuration as the initial condition. The first voltage pulse induces a positive IEC peak (corresponds to  $P_4$ ) and switches the free magnet to an AFM configuration with respect to the fixed magnet. The AFM configuration is retained when the voltage pulse

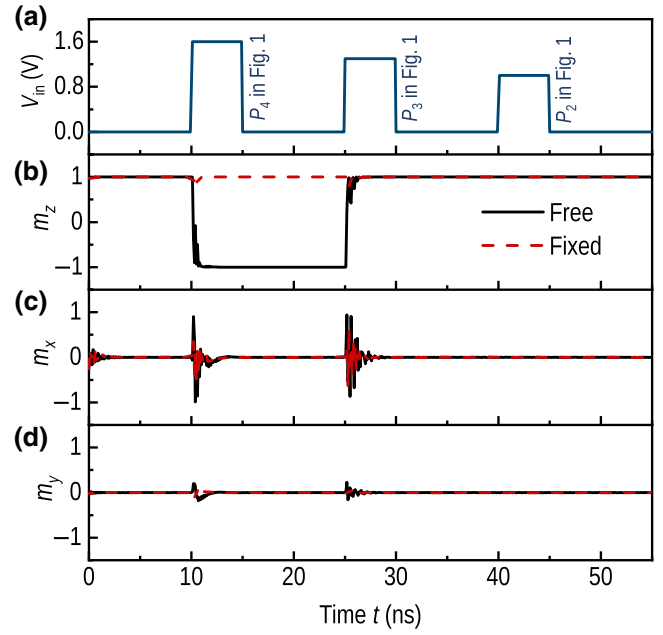


FIG. 3. (a) Voltage pulse applied across the structure in Fig. 1(a). The three voltage pulses applied induce IEC with strengths corresponding to  $P_4$ ,  $P_3$ , and  $P_2$ , respectively, in Fig. 1(b). We observe the magnetization dynamics as a function of time, as a result of the applied voltage pulses: (b)  $z$  component  $m_z$ , (c)  $x$  component  $m_x$ , and (d)  $y$  component  $m_y$ . Fixed magnet:  $M_{s1} = 1100$  emu/cc,  $H_{k1} = 300$  Oe, and  $t_{f1} = 10$  ns. Free magnet:  $M_{s2} = 1100$  emu/cc,  $H_{k2} = 150$  Oe, and  $t_{f2} = 1.5$  ns. Diameter of the device is 150 nm and the Gilbert damping is 0.01.

is removed because of the negligible equilibrium IEC in the structure. The second voltage pulse induces a negative IEC peak (corresponds to  $P_3$ ), which switches the free magnet back to a FM configuration with respect to the fixed magnet. Again, the FM configuration is retained when the voltage pulse is removed. Note that the switching in both directions is achieved for the same voltage polarity but different magnitudes, which is very different from existing mechanisms for electrical switching. The rise time and the fall time of these switching voltage pulses should be lower than the switching time [see Eq. (6)], in order to avoid any unexpected switching. The third voltage pulse induces another positive IEC peak (corresponds to  $P_2$ ), however, the IEC strength  $|J_{\text{ex}}|$  is weak enough such that the free magnet does not switch. The threshold for the IEC-driven magnetization switching is discussed below [see Eq. (5)].

#### 1. Switching threshold

The threshold value of the IEC energy required for magnetization switching ( $|J_{\text{ex}0}|$ ) is given by

$$|J_{\text{ex}0}| \times S = \frac{2E_1E_2}{E_1 + E_2}, \quad (5)$$

where  $S$  is the cross-section area of the device,  $E_1$  and  $E_2$  are the anisotropy energy barriers of the fixed and the free magnets, respectively.  $E_{1,2}$  are determined by  $\frac{1}{2}M_s H_k \Omega$  of the corresponding magnet, where  $M_s$  is the saturation magnetization,  $H_k$  is the anisotropy field, and  $\Omega$  is the magnet volume. Equation (5) is derived from an exchange-coupled LLG model [50,51], considering only IEC as the external excitation. Details are given in Appendix B. The fixed magnet is set by making the anisotropy energy much larger than the free magnet:

$$E_1 > E_2.$$

Equation (5) is valid for magnets with both in-plane and perpendicular magnetic anisotropies and independent of the demagnetizing field. Moreover, the threshold energy is independent of the Gilbert damping. These features are different from the conventional spin-torque devices [52], where the threshold energy of the nonequilibrium spin current scales with the Gilbert damping and the demagnetizing field. This is because the exerted torque ( $\vec{\tau}$ ) by the IEC energy is equivalent to an external magnetic-field-driven torque, which is conservative in nature ( $\vec{\nabla}_m \times \vec{\tau} = 0$ ). See Appendix C for details. On the other hand, the torque exerted by a nonequilibrium spin current is nonconservative in nature ( $\vec{\nabla}_m \times \vec{\tau} \neq 0$ ), as previously discussed in Ref. [53].

## 2. Switching time

The IEC-assisted switching time is given by

$$t_{\text{sw}} = \frac{1 + \alpha_g^2 |J_{\text{ex}0}|}{\alpha_g \gamma H_k |J_{\text{ex}}|}, \quad (6)$$

where  $\gamma$  is the gyromagnetic ratio and  $\alpha_g$  is the Gilbert damping. Equation (6) is obtained from an exchange-coupled LLG model [50,51], assuming magnets with perpendicular anisotropy. We define the switching time as the time taken by the free magnet to settle down to a magnetic state, when the sign of the  $J_{\text{ex}}$  is reversed to make the configuration unstable, given that  $|J_{\text{ex}}| > J_{\text{ex}0}$ . We also assume that the magnets have comparable  $H_k$ , and their anisotropy energies differ by the difference in the total magnetic moment. The details of the derivation and comparison with the numerical simulations based on the LLG model is provided in Appendix B. Note that magnets with in-plane anisotropies should be relatively faster due to the presence of a demagnetizing field, which can be analyzed directly from the coupled LLG model.

The functional dependence of the IEC-induced switching time on  $\alpha_g$  and  $H_k$  are similar to that observed in conventional spin-torque devices [52]. Two distinct differences are as follows: (i) the IEC switching time scales inversely with an over-drive factor  $|J_{\text{ex}}|/|J_{\text{ex}0}|$ , while the

spin-torque switching time scales inversely with similar over-drive factor  $|J_s|/|J_{s0}| - 1$  [52] ( $J_s$ , applied spin current density;  $J_{s0}$ , switching threshold); and (ii) the IEC-induced switching mechanism is not limited by the initial angle requirements as seen in spin-torque switching [52]. The switching takes place even if the magnets are perfectly aligned (i.e., initial angle = 0).

The decoupling of the switching threshold and the speed, in terms of the Gilbert damping and the demagnetizing field may offer some advantages over conventional spin-torque devices in terms of the energy-delay product (see Appendix B). In particular, because the spin-torque devices exhibit a well-known trade-off between the threshold and the speed in terms of these dynamic parameters [52]. The estimated write energy of the proposed device using the calibrated material parameters is approximately 5.76 fJ and the write speed is approximately 1 ns, which are much lower than the conventional STT MRAM [15]. The estimated speed of the proposed device is similar to that observed in typical static RAM, and the estimated write energy is lower than that observed in typical dynamic RAM for embedded applications (see Appendix B).

## B. Signature of the electric-field-induced IEC

We simulate the total magnetic moment  $M$  of the device as a function of an external magnetic field sweep  $H_{\text{ext}}$  ( $M$ - $H$  loops in Fig. 4), for different applied voltages  $V_{\text{in}}$ . The  $y$  axes of Fig. 4 are normalized with  $M_0 = M_{s1}\Omega_1 + M_{s2}\Omega_2$ , where  $M_{s1,2}$  and  $\Omega_{1,2}$  are the saturation magnetizations and volumes of the fixed and the free layers. For structures with two ferromagnets separated by a thin spacer layer, such  $M$ - $H$  loops are typically measured to estimate the equilibrium IEC between the two magnets [27,29,30]. The presence of an IEC causes a shift in the switching field of the magnets.

We expect a similar signature of the resonant enhancement of IEC in the  $M$ - $H$  loops of the REC MRAM device, where the total spacer thickness is fixed. A change in the  $M$ - $H$  loops will occur for different  $V_{\text{in}}$ , as described below. In our simulations, the rate of the  $H_{\text{ext}}$  sweep is slow enough that the magnetization of the both layers reach the steady state, as typically done in experiments.  $J_{\text{ex}}$  is negligible in our structure at equilibrium [i.e.,  $V_{\text{in}} = 0$  V,  $P_1$  in Fig. 1(b)], and the  $M$ - $H$  loop is such that the two magnets are switching at the corresponding coercive fields [see Fig. 4(a)]. Here,  $H_{k1} = 300$  Oe for the fixed magnet and  $H_{k2} = 150$  Oe for the free magnet in the simulations.  $|M| = |M_{s1}\Omega_1 + M_{s2}\Omega_2|$  when the magnets are parallel and  $|M| = |M_{s1}\Omega_1 - M_{s2}\Omega_2|$  when they are antiparallel.

At  $V_{\text{in}} = 1$  V, we observe the first voltage-induced AFM positive peak of  $+0.012$  mJ/m<sup>2</sup> [ $P_2$  in Fig. 1(b)]. This AFM coupling exhibits as a lowering of the switching field of the free magnet as shown in Fig. 4(b). As mentioned earlier, the strength of the IEC at  $P_2$  is below the switching

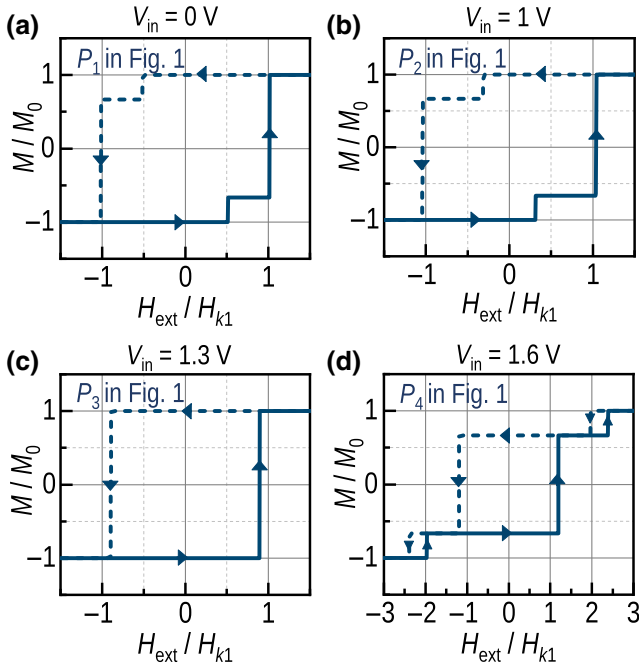


FIG. 4.  $M$ - $H$  loop of the structure in Fig. 1 for different applied voltages  $V_{\text{in}}$ : (a) 0 V [corresponds to  $P_1$  in Fig. 1(b)], (b) 1 V (corresponds to  $P_2$  in Fig. 1(b)), (c) 1.3 V [corresponds to  $P_3$  in Fig. 1(b)], and (d) 1.6 V [corresponds to  $P_4$  in Fig. 1(b)]. Fixed magnet:  $M_{s1} = 1100$  emu/cc,  $H_{k1} = 300$  Oe, and  $t_{f1} = 10$  nm. Free magnet:  $M_{s2} = 1100$  emu/cc,  $H_{k2} = 150$  Oe, and  $t_{f2} = 1.5$  nm. The diameter is 150 nm and the Gilbert damping is 0.01.

threshold [in Eq. (5)], however, it should still be exhibited in the  $M$ - $H$  loop as discussed above. At  $V_{\text{in}} = 1.3$  V, we observe the negative FM peak of  $-0.08$  mJ/m<sup>2</sup> [ $P_3$  in Fig. 1(b)] and the  $M$ - $H$  loop exhibits a rectangular shape [see Fig. 3(d)]. Such a rectangular shape is a well-known evidence for a FM-type IEC coupling [27,29,30], indicating that the magnets are switching simultaneously and net magnetic moment is  $|M| = |M_{s1}\Omega_1 + M_{s2}\Omega_2|$ . At  $V_{\text{in}} = 1.6$  V, we observe another positive AFM peak [ $P_4$  in Fig. 1(c)], the strength of which is above the switching threshold. The  $M$ - $H$  loop, in this case, exhibits a large split due to a large shift in the free-magnet switching field. At low field ( $|H_{\text{ext}}| < \sim H_{k1}$ ), the magnets are antiparallel due to the strong AFM IEC, so the net moment is  $|M| = |M_{s1}\Omega_1 - M_{s2}\Omega_2|$ . The fixed layer is switched approximately  $H_{k1}$  and the free layer switches as well to stay antiparallel due to the strong AFM IEC. So the total moment still remains  $|M| = |M_{s1}\Omega_1 - M_{s2}\Omega_2|$ . At very large  $H_{\text{ext}}$ , both magnets align with the external field and the total moment becomes  $|M| = |M_{s1}\Omega_1 + M_{s2}\Omega_2|$ .

#### IV. DISCUSSION ON THE DEVICE DESIGN

In this section, we discuss various design aspects of the REC MRAM. As discussed in the previous section, the switching speed or delay can be optimized using dynamic

parameters like Gilbert damping and demagnetizing field, while the IEC switching threshold energy remains unaffected. We can design a structure that can induce a significant enhancement in IEC with an electric field such that  $|J_{\text{ex}}| > |J_{\text{ex}0}|$ , while the current density  $J_c$  of the structure can be significantly lower. Moreover, the QW shape can be changed to set the operating voltages.

#### A. Resonance-enhanced exchange coupling

The IEC strength is determined by the occupied electronic states within the spacer layer [33,34]. As seen from Eqs. (1)–(3), IEC depends on  $\vec{\sigma} G^n$ , which is related to the spin density in the spacer.  $\vec{\sigma} G^n$  can be written as a sum of the following two components:

$$\vec{\sigma} G^n = \vec{\sigma} A \frac{f_1 + f_2}{2} + \vec{\sigma} (A_1 - A_2) \frac{f_1 - f_2}{2}, \quad (7)$$

where  $A = A_1 + A_2$  is the total spectral function and related to the density of states of the spacer.  $f_1$  and  $f_2$  are the Fermi occupation factors of the left and the right contacts, respectively. Hence, the first term in Eq. (7) represents the filled electronic states and nonzero even at equilibrium (i.e.,  $f_1 = f_2$ ). A spacer having a large density of states and a high spin-dependent mismatch with the magnet is an ideal choice for the REC MRAM device, in order to achieve a voltage-induced IEC with large magnitude. For higher voltages where the conduction is expected to have a component due to the bulk density of states, we observe that the magnitude of the resonance-enhanced IEC is growing [see Fig. 1(b)], because the magnitude is determined by the occupied states and the spin-dependent quantum interference of the wave functions controlled by the resonant tunneling. The change of the IEC sign depends on the nature of the interference pattern, as discussed earlier.

The voltage-dependent oscillation in the resonance-enhanced IEC [see Fig. 1(b)] shows a sinusoidal behavior that is increasing in magnitude with the input voltage. The origin of the sinusoidal nature as a function of the input voltage is the same as the origin of the sinusoidal nature as a function of the spacer thickness at equilibrium, which is the quantum interference of the spin-dependent wave functions due to a reflection from the magnetic interfaces (see, e.g., Refs. [32–34]). In our device, we are simply controlling the transmission coefficient of the wave functions using  $V_{\text{in}}$ . The periodicity of the voltage-dependent oscillation in IEC ( $V_{\text{REC}}$ ) is directly related to the equilibrium periodicity of the spacer ( $\lambda_{\text{IEC}}$ ), determined by  $\Delta_{\text{sp}}$ .  $V_{\text{REC}}$  scales with the spacer property  $\lambda_{\text{IEC}}$  as shown in Fig. 5(a). A device with large  $V_{\text{REC}}$  can be achieved with a spacer with large  $\lambda_{\text{IEC}}$ . The resonance-enhanced IEC is robust to the incoherent elastic scattering with momentum and phase-relaxation processes, as shown in Fig. 5(b). Both the periodicity and the magnitude are unaffected by the presence of a dephasing ( $d_{\text{ph}}$ ) in the device. A similar

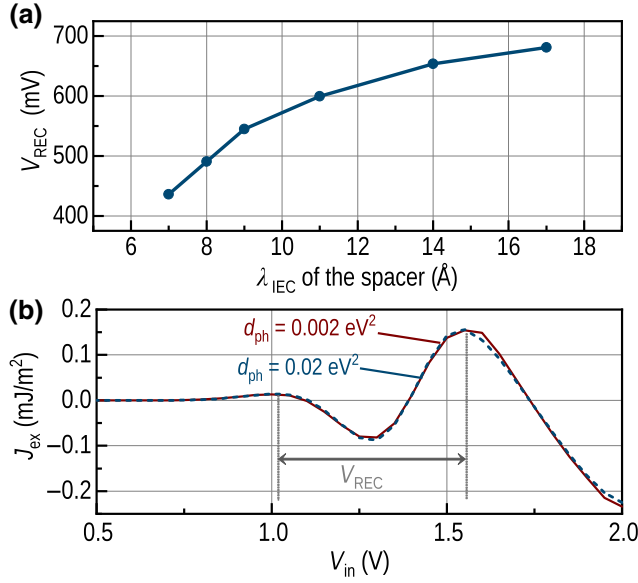


FIG. 5. (a) Voltage periodicity ( $V_{\text{REC}}$ ) of the resonance-enhanced IEC, which scales with the equilibrium periodicity ( $\lambda_{\text{IEC}}$ ) of the spacer (determined by  $\Delta_{\text{sp}}$ ). (b) Effect of dephasing ( $d_{\text{ph}}$ ) on the resonance-enhanced IEC.

observation has been discussed in the past [54] using the NEGF method that the spin-dependent resonant tunneling is robust against dephasing in a magnetic tunnel junction.

### B. Current and magnetoresistance

The magnitude of the charge current is limited by the electronic states positioned within the window created by the separation between the contact Fermi levels. We calculate the charge-current density  $J_c$  and the  $z$ -polarized spin-current density  $J_z$  of the structure in Fig. 1(a), as

$$J_c = \int d\epsilon_T D_0 \left( \int dE \text{Re} \{ \text{Tr} [I_{\text{op}}(E)] \} \right), \quad (8a)$$

$$\text{and } J_z = \int d\epsilon_T D_0 \left( \int dE \text{Re} \{ \text{Tr} [\sigma_z I_{\text{op}}(E)] \} \right), \quad (8b)$$

with

$$I_{\text{op}}(E) = \frac{q}{i\hbar} (HG^n - G^nH).$$

Here,  $H$  is the Hamiltonian of the structure. The calculated  $J_c$  and  $J_z$  are shown in Fig. 6(a). The details are provided in Appendix A. We observe a bias-dependent oscillation in the current density as a function of voltage, which is a signature of the resonant tunneling. The peaks observed in  $J_c$  correspond to high transmission coefficient across the barriers, mediated by the QW states. We observe two sharp peaks of width approximately 90 mV at input voltage  $< 0.75$  V.

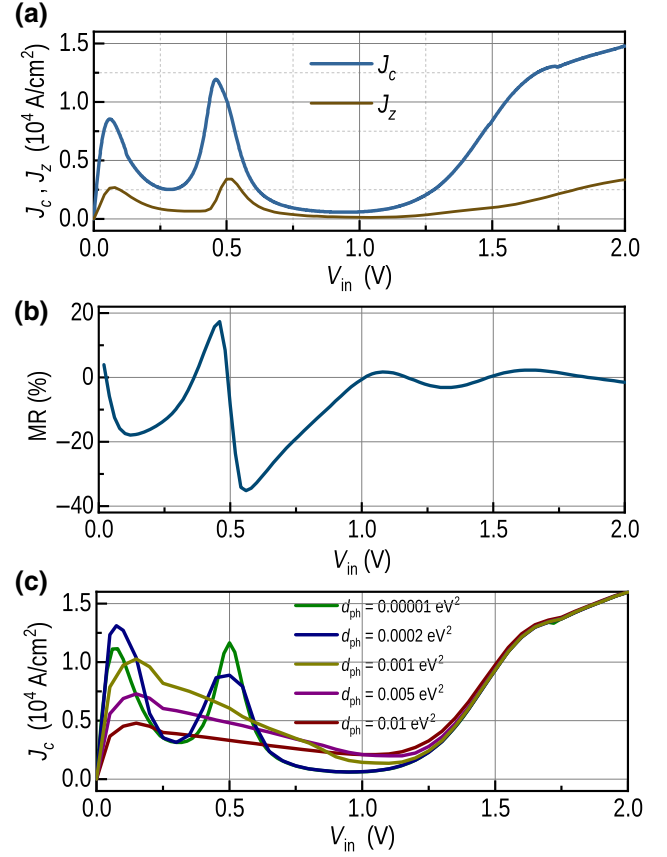


FIG. 6. (a) Charge and  $z$ -polarized spin-current densities,  $J_c$  and  $J_z$ , as a function of the applied voltage  $V_{\text{in}}$ . (b) Magnetoresistance as a function of  $V_{\text{in}}$ . (c) Effect of dephasing ( $d_{\text{ph}}$ ) on the current transport.

The calculated charge-current density in the structure is small within the voltage range of interest, in the order of approximately  $10^4$  A/cm<sup>2</sup>. The charge-current density induces a  $z$ -polarized (parallel to the magnetization) spin-current density of order approximately  $10^3$  A/cm<sup>2</sup>, which is much smaller than the threshold value for STT switching. For the free magnet under consideration, the switching threshold for the spin-current density is approximately  $3.6 \times 10^6$  A/cm<sup>2</sup> using  $J_{s0} = (2q/\hbar)M_{s2}t_f \alpha_g (H_{k2} + 2\pi M_{s2})$  [52]. Bidirectional switching in REC MRAM is achieved with the same voltage polarity, hence  $J_z$  is always acting in the same direction. Thus  $J_z$  will help the switching in one direction and oppose it for the other direction. However, such an effect from STT on switching is negligible in the present discussion since  $J_z$  is 3 orders lower than the STT switching threshold.

We further calculate the structure resistance  $R$  when the magnets are in AFM and FM configurations, respectively. We estimate the magnetoresistance of the structure  $(R_{\text{AFM}} - R_{\text{FM}})/R_{\text{AFM}}$  for the same simulation parameter



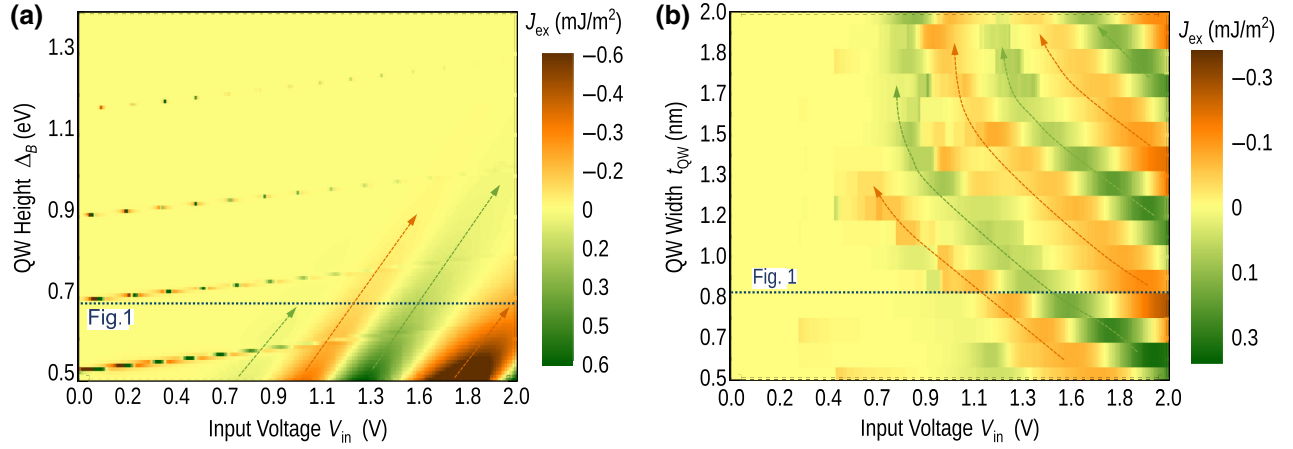


FIG. 7. Voltage-dependent oscillatory resonance-enhanced IEC for different (a) QW heights  $\Delta_B$  and (b) QW widths  $t_{QW}$ .

set, as shown in Fig. 6(b). Interestingly, the MR shows oscillation with a change in sign. The negative MR corresponds to a scenario where  $R_{AFM}$  is lower than  $R_{FM}$  assisted by the QW states. A similar voltage-dependent oscillation in MR with a sign reversal, due to the resonant tunneling has been reported in the past [22–26]. Our calculated MR is small (20%~35%) for the materials combination considered here. Further enhancement in MR is possible using different materials combination and superlattice-based resonant-tunneling structures (see, e.g., Refs. [55–57]), which we do not consider in the present work.

One interesting observation is that the MR is decreasing as a function of the voltage [see Fig. 6(b)], while the IEC strength is increasing [see Fig. 1(b)]. This feature is very interesting for memory applications since we have reasonable MR for lower voltage (where the induced  $|J_{ex}| < |J_{ex0}|$ ). No switching will occur in this region and can be designated as the operating voltage for the read operation. The writing is enabled by higher voltages where the induced  $|J_{ex}| > |J_{ex0}|$ . One thing to be noted is that a pure electric-field-controlled device has a very high baseline resistance and a proper scheme for readout such as the gain cell structure will be needed [58].

We also analyze the effect of dephasing ( $d_{ph}$ ) on the current transport of the device. Here,  $d_{ph}$  induces incoherent elastic scatterings that enable momentum and phase relaxation. For low  $d_{ph}$ , we see that the two resonant peaks below 0.75 V is unchanged. For increased  $d_{ph}$ , we observe a change in the shapes of the two resonant peaks and they start broadening. Further broadening with increasing  $d_{ph}$  merges the two peaks and the magnitude of the merged peak decreases for very high values of  $d_{ph}$ . Note that even for a very large  $d_{ph}$ , we still observe the negative differential resistance in the current-voltage characteristics, which is a key signature of the resonant tunneling.

### C. QW dimensions and the operating voltage

The charge current in the structure can be further decreased by using a different oxide material with larger barrier height, e.g.,  $Al_2O_3$ ,  $HfO_2$ ,  $SiO_2$ ,  $TiO_2$ , etc. We analyze the effect of different barrier heights on the resonance-enhanced IEC in the proposed REC MRAM, as shown in Fig. 7(a). Figure 7(a) shows the oscillatory nature of the resonance-enhanced IEC as a function of  $V_{in}$ . The IEC strength at lower  $V_{in}$  gets diminished for higher barrier heights and the voltage-dependent oscillatory IEC shifts toward the higher operating voltages as we increase the barrier height. We also note from our simulations that for a given barrier height, an additional sharp oscillation peak can be observed at lower operating voltages, which occurred due to a small mismatch of transmission coefficients for the parallel and the antiparallel configurations. This sharp oscillation shifts toward higher operating voltages linearly with the increasing barrier height and periodically reoccurs at the lower voltages.

We also analyze the effect of the spacer-metal thickness on the resonance-enhanced IEC, as shown in Fig. 7(b). It is interesting to note that the oscillation peaks occur at lower operating voltages for a thicker spacer layer, but the strength of the peaks decreases as well. The former is observed because the spacer-layer thickness defines the QW width. An increase in the QW width lowers the discrete energy states as well as the spacing between two consecutive states. Thus the operating voltage to observe an IEC peak decreases with increasing spacer thickness. Similar lowering of the QW energy states for wider QW and its consequence on the operating voltage has been discussed for double-barrier MTJs [23]. The later observation is due to the increasing distance between two magnets, which causes the IEC to weaken. Similar weakening of the IEC strength with increasing distance between the magnets

has been discussed both theoretically and experimentally in the past [27–29,32–34].

## V. SUMMARY

We proposed a structure that enables electric-field-controlled magnetization switching assisted, solely by the interlayer exchange coupling between the fixed and the free magnets. The two magnets are separated by two oxide barriers sandwiching a metallic spacer and the basic idea relies on a quantum-well formation within the spacer. When the contact electrochemical potential is aligned with one of the discrete states in the quantum well, the two magnets feel a strong IEC due to an enhanced transmission coefficient across the structure stemming from resonant tunneling. IEC shows an oscillation in sign as a function of the applied voltage and the magnitude is determined by the filled electronic states. Such oscillatory IEC can enable bidirectional switching for the same voltage polarity but different magnitudes above the switching threshold value. We show that the switching threshold of the proposed mechanism is decoupled from the speed, because the torque exerted by the IEC is conservative. This is fundamentally different from the conventional spin-torque devices where there is a well-known trade-off between the threshold and the speed due to the nonconservative nature of the exerted torque. We further show that the structure exhibits an oscillation in the magnetoresistance due to the resonant tunneling, and a reasonably large MR can be achieved for voltages lower than the switching threshold. The proposed structure is promising for nonvolatile memory application and could enable lower energy-delay product as compared to the conventional mechanisms.

## ACKNOWLEDGMENTS

This work is in part supported by ASCENT, one of six centers in JUMP, a SRC program sponsored by DARPA and in part by the Center for Energy Efficient Electronics Science (E3S), NSF Award 0939514.

## APPENDIX A: NEGF MODEL

This appendix discusses the nonequilibrium Green's function (NEGF) method [46,59] used for quantum-transport simulations presented in this paper.

### 1. Hamiltonian

We write the tight-binding Hamiltonian of the structure as the following:

$$[\beta]^\dagger \Psi(n-1) + [\alpha] \Psi(n) + [\beta] \Psi(n+1) = E \Psi(n), \quad (\text{A1})$$

where  $\Psi(n)$  is the wave function of the  $n$ th lattice point along the  $y$  direction. We work with a single-band

effective-mass Hamiltonian, described by (1) the equilibrium Fermi level  $E_F$ , (2) exchange splitting  $\Delta_{\text{ex}}$ , (3) barrier height  $\Delta_B$ , (4) well depth  $\Delta_{\text{sp}}$ , (5) effective mass for ferromagnet layer  $m_f^*$  (we assume equal effective mass for up and down spin polarized electrons, i.e.,  $m_{f\uparrow}^* = m_{f\downarrow}^* = m_f^*$ ), (6) effective mass for oxide layer  $m_{\text{ox}}^*$ , (7) effective mass for metallic spacer  $m_n^*$ , and (8) contact electrochemical potentials  $\mu_{1,2}$ . Note that we view these parameters to take into account wide varieties of factors like imperfection at the ferromagnet-nonmagnet interfaces, because we calibrate the parameters using various room-temperature experiments. We assume that the structure under consideration is spatially uniform along the transverse directions and transverse modes are nearly decoupled so that transport can be analyzed with a 1D Hamiltonian for every mode. Below, we present Hamiltonian for each transverse mode with wave vector  $k_{\parallel}$  in the device.

### a. Ferromagnetic layers

For the lattice points within the ferromagnetic layers (indicated by region-1 in Fig. 8), we have

$$[\alpha] = \left[ 2t_f + \frac{\hbar^2 k_{\parallel}^2}{2m_f^*} + qV(n) \right] I_{2 \times 2} + \frac{\Delta_{\text{ex}}}{2} (I - \vec{\sigma} \cdot \vec{m}), \quad (\text{A2a})$$

$$[\beta] = -t_f I_{2 \times 2}, \quad (\text{A2b})$$

with  $t_f = \hbar^2/2m_f^*a^2$ ,  $k_{\parallel}$  is the transverse wave vector,  $I_{2 \times 2}$  is a  $2 \times 2$  identity matrix,  $\vec{\sigma}$  is the Pauli spin matrices, and  $a$  is the lattice distance. Here,  $qV(n)$  is the potential on the  $n$ th lattice point of the structure. The potential is varied by the applied voltage  $V_{\text{in}}$  across the structure, which drops across each layer according to the resistance of each layer, as shown in Fig. 8.  $\vec{m}_1$  and  $\vec{m}_2$  are the magnetization vectors of the fixed and the free magnet, respectively. Note that in Eq. (A2a),  $\vec{m} = \vec{m}_1$  for fixed-magnet region and  $\vec{m} = \vec{m}_2$  for free-magnet region.

### b. Oxide layers

For the lattice points within the oxide layers (indicated by regions 2 in Fig. 8), we have

$$[\alpha] = \left[ 2t_{\text{ox}} + \frac{\hbar^2 k_{\parallel}^2}{2m_{\text{ox}}^*} + \Delta_B + qV(n) \right] I_{2 \times 2}, \quad (\text{A3a})$$

$$[\beta] = -t_{\text{ox}} I_{2 \times 2}, \quad (\text{A3b})$$

with  $t_{\text{ox}} = \hbar^2/2m_{\text{ox}}^*a^2$ .

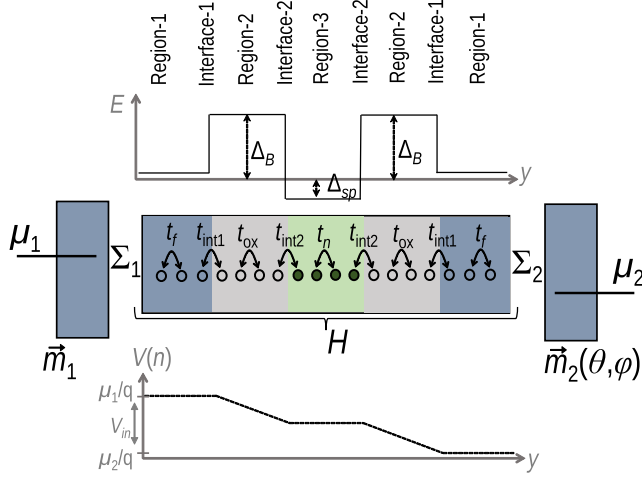


FIG. 8. NEGF setup for the structure in Fig. 1(a).

### c. Spacer layer

For the lattice points within the metallic spacer layer (indicated by region 3 in Fig. 8), we have

$$[\alpha] = \left[ 2t_n + \frac{\hbar^2 k_{\parallel}^2}{2m_n^*} - \Delta_{\text{sp}} + qV(n) \right] I_{2 \times 2}, \quad (\text{A4a})$$

$$[\beta] = -t_n I_{2 \times 2}, \quad (\text{A4b})$$

with  $t_n = \hbar^2/2m_n^*a^2$ , and  $\Delta_{\text{sp}}$  is the depth of the spin-dependent QW-like potential below  $E_F$ .

### d. Ferromagnet-oxide interfaces

For the lattice points at the interface between the ferromagnet and oxide layers (indicated by interface-1 in Fig. 8), we have

$$[\alpha] = \left[ t_f + t_{\text{ox}} + \frac{\hbar^2 k_{\parallel}^2}{4m_f^*} + \frac{\hbar^2 k_{\parallel}^2}{4m_{\text{ox}}^*} + \frac{\Delta_B}{2} + qV(n) \right] I_{2 \times 2} + \frac{\Delta_{\text{ex}}}{4} (I - \vec{\sigma} \cdot \vec{m}), \quad (\text{A5a})$$

$$[\beta] = 0, \quad (\text{A5b})$$

where  $\vec{m} \equiv \vec{m}_1$  for the interface 1 on the left and  $\vec{m} \equiv \vec{m}_2$  is for the interface 1 on the right.

### e. Oxide-spacer interfaces

For the lattice points at the interface between the oxide and the spacer layers (indicated by interface-2 in Fig. 8),

we have

$$[\alpha] = \left( t_{\text{ox}} + t_n + \frac{\hbar^2 k_{\parallel}^2}{4m_{\text{ox}}^*} + \frac{\hbar^2 k_{\parallel}^2}{4m_n^*} \right) I_{2 \times 2} + \left[ \frac{\hbar^2 k_{\parallel}^2}{4m_n^*} + \frac{\Delta_B + \Delta_{\text{sp}}}{2} + qV(n) \right] I_{2 \times 2}. \quad (\text{A6})$$

## 2. Self-energy of contacts

We present self-energy matrices for each transverse mode with wave vector  $k_{\parallel}$  in the device. The self-energy matrices are given by

$$\Sigma_{1,2} = \begin{bmatrix} -t_f e^{ik_{1,2}^{\uparrow} a} & 0 \\ 0 & -t_f e^{ik_{1,2}^{\downarrow} a} \end{bmatrix}, \quad (\text{A7})$$

where  $k_{1,2}^{\uparrow}$  and  $k_{1,2}^{\downarrow}$  are longitudinal wavevectors of up and down spins, respectively, which are calculated from

$$E = E_{C,1}^{\uparrow,\downarrow} + \frac{qV_{\text{in}}}{2} + \frac{\hbar^2 k_{\parallel}^2}{2m_f^*} + 2t_f \left[ 1 - \cos(k_{1,2}^{\uparrow,\downarrow}) \right], \quad (\text{A8a})$$

$$E = E_{C,2}^{\uparrow,\downarrow} - \frac{qV_{\text{in}}}{2} + \frac{\hbar^2 k_{\parallel}^2}{2m_f^*} + 2t_f \left[ 1 - \cos(k_{2,1}^{\uparrow,\downarrow}) \right], \quad (\text{A8b})$$

with  $E_{C,1}$  and  $E_{C,2}$  being the bottom of the conduction bands for left and right magnetic contacts.

In the present discussion, the magnetization  $\vec{m}_2$  of the free magnet can lie in an arbitrary direction, hence, the effective  $\Sigma_2$  is given by

$$\Sigma_2 = R_m(\theta, \phi) \begin{bmatrix} -t_f e^{ik_2^{\uparrow} a} & 0 \\ 0 & -t_f e^{ik_2^{\downarrow} a} \end{bmatrix} R_m^{\dagger}(\theta, \phi), \quad (\text{A9})$$

with  $R_m(\theta, \phi)$  being a rotational matrix given by

$$R_m(\theta, \phi) = \begin{bmatrix} \cos \frac{\theta}{2} e^{-i\frac{\phi}{2}} & -\sin \frac{\theta}{2} e^{-i\frac{\phi}{2}} \\ \sin \frac{\theta}{2} e^{+i\frac{\phi}{2}} & \cos \frac{\theta}{2} e^{+i\frac{\phi}{2}} \end{bmatrix}. \quad (\text{A10})$$

## 3. NEGF quantities

We calculate the following quantities:

(a) Green's function:

$$G^R = [EI - H - \Sigma]^{-1}, \quad (\text{A11})$$

with  $\Sigma = \Sigma_1 + \Sigma_2 + \Sigma_0$  [see Eqs. (A7) and (A9)].  $\Sigma_0$  represents incoherent scattering processes (see Appendix A4).

$H$  is the Hamiltonian of the system as discussed earlier and  $I$  is an identity matrix.

(b) Spectral function:

$$A = G^R \Gamma (G^R)^\dagger, \quad (\text{A12})$$

with  $\Gamma = \Gamma_1 + \Gamma_2 + \Gamma_0$  and  $\Gamma_{1,2}$  are broadening functions, which represent the anti-Hermitian part of  $\Sigma_{1,2}$ , i.e.,  $\Gamma_{1,2} = i(\Sigma_{1,2} - \Sigma_{1,2}^\dagger)$ .  $\Gamma_0$  represents incoherent scattering processes (see Appendix A4). Note that  $A/2\pi$  provides the density of states of the system.

(c) Correlation function:

$$G^n = G^R \Sigma^{\text{in}} (G^R)^\dagger, \quad (\text{A13})$$

with  $\Sigma^{\text{in}} = \Sigma_1^{\text{in}} + \Sigma_2^{\text{in}} + \Sigma_0^{\text{in}}$  being the in-scattering function.  $\Sigma_0^{\text{in}}$  represents incoherent scattering processes (see Appendix A4). Note that  $G^n/2\pi$  provides the electron density of the system.

(d) In-scattering function:

$$\Sigma_{1,2}^{\text{in}} = \Gamma_{1,2} f_{1,2}, \quad (\text{A14})$$

with  $f_{1,2}$  being the Fermi occupation factors of contacts 1 and 2, given by

$$f_{1,2} = \frac{1}{1 + \exp\left(\frac{E - \mu_{1,2}}{k_B T}\right)}. \quad (\text{A15})$$

Here,  $\mu_{1,2}$  are electrochemical potentials of contacts 1 and 2,  $k_B$  is the Boltzmann constant, and  $T$  is the temperature. In the present discussion,  $qV_{\text{in}} = \mu_1 - \mu_2$  and  $T = 300$  K.

(e) Current operator:

$$I^{\text{op}} = \frac{q}{i\hbar} (HG^n - G^n H). \quad (\text{A16})$$

Current operator between two adjacent lattice points  $j$  and  $j + 1$  is given by

$$I_{j,j+1}^{\text{op}} = \frac{q}{i\hbar} (H_{j,j+1} G_{j,j+1}^n - G_{j,j+1}^n H_{j,j+1}). \quad (\text{A17})$$

The charge-current density per mode is given by

$$J_c^m = \int dE \text{Re} \left[ \text{Tr} \left( I_{j,j+1}^{\text{op}} \right) \right]. \quad (\text{A18})$$

The spin-current density per mode is given by

$$\vec{J}_s^m = \int dE \text{Re} \left[ \text{Tr} \left( \vec{\sigma} I_{j,j+1}^{\text{op}} \right) \right]. \quad (\text{A19})$$

The total charge-current density and spin-current density are given by

$$J_c = \int d\epsilon_T D_0 J_c^m \quad \text{and} \quad (\text{A20a})$$

$$\vec{J}_s = \int d\epsilon_T D_0 \vec{J}_s^m, \quad (\text{A20b})$$

where  $\epsilon_T = \hbar^2 (k_y^2 + k_z^2)/2m^*$  is the energy along the transverse plane  $z$ - $x$  and  $D_0$  is the 2D density of states on the transverse plane.

We approximate  $D_0$  with the 2D density of states of the bulk given by [46]

$$D_0 = \frac{m^*}{\pi \hbar^2}, \quad (\text{A21})$$

where  $m^*$  is the effective mass and  $\hbar = h/2\pi$ .

#### 4. Dephasing

We include incoherent scattering with isotropic momentum and phase relaxation in terms of a dephasing parameter  $d_{\text{ph}}$ . The self-energy and in-scattering functions are given by

$$(\Sigma_0)_{ij} = d_{\text{ph}} \delta_{ij} \delta_{ik} \delta_{jl} (G^R)_{kl}, \quad (\text{A22a})$$

$$(\Sigma_0^{\text{in}})_{ij} = d_{\text{ph}} \delta_{ij} \delta_{ik} \delta_{jl} (G^n)_{kl}, \quad (\text{A22b})$$

where  $\delta$  is the Kronecker delta function.

All the NEGF simulations presented in this paper do not take into account dephasing. We separately evaluate the effect of the momentum and the phase-relaxation processes on the resonant tunneling and the resonance-enhanced IEC for the structure in Fig. 1(a). For variable dephasing strengths, we do not observe any change in the resonance-enhanced IEC [see Fig. 5(b)]. A similar robustness of the spin-based resonant tunneling against dephasing in a magnetic tunnel junction has been discussed in the past [54] using the NEGF method. We observe a broadening of the sharp current density peaks for very large dephasing [see Fig. 6(c)]. However, the negative differential resistance is observed even for large dephasing, which is a key indicator that the resonant tunneling is occurring.

#### 5. IEC calculation

We start by calculating the  $z$ -spin density at the interfaces as

$$n_{z,j}^{1D} = \text{Re} \left[ \text{Tr} \left( \sigma_z G_{j,j+1}^n \right) \right], \quad (\text{A23})$$

where  $\sigma_z$  is the  $z$ -Pauli matrix, and  $G^n$  is the correlation function. We assume that the structure under consideration is spatially uniform along the transverse directions



and transverse modes are nearly decoupled so that transport can be analyzed with 1D Hamiltonian for every mode. Under such an assumption, we do a mode summation on the transverse plane ( $z$ - $x$  plane), to estimate the 2D  $z$ -spin density at  $j$ th lattice point, as given by

$$n_s(y_j) = \frac{1}{2\pi} \int D_0 n_{zj}^{1D} d\epsilon_T, \quad (\text{A24})$$

where  $\epsilon_T = \hbar^2 (k_y^2 + k_z^2)/2m^*$  is the energy along the transverse plane  $z$ - $x$ , and  $D_0$  is given by Eq. (A21).

The change in  $z$ -spin density across the QW is given by

$$\Delta n_s = n_s(y_j = 0) - n_s(y_j = t_{\text{QW}}). \quad (\text{A25})$$

The total change in energy of the occupied states across the QW is calculated as

$$\Delta E = \int_{-\infty}^{+\infty} E \Delta n_s(E) dE, \quad (\text{A26})$$

which is in the units of  $\text{J}\cdot\text{m}^{-2}$ .

In a magnetic structure, the IEC energy density is given by Eq. (1) [32–34]

$$J_{\text{ex}} = \Delta E_{\text{FM}} - \Delta E_{\text{AFM}}.$$

The parameters used in this paper are listed in Table I. The energy grid used for numerical integration has been optimized by finding the sharpest resonance peak for a given parameter set. For the parameter set discussed here, the energy width (width calculated at half of the resonant peak) of the sharper peak is around approximately 0.02 eV. The energy spacing selected is approximately 50 times smaller than this width. For calculation of IEC, a large energy range is chosen as the integration limit such that the integral based on the spin-dependent mismatch does not show any noticeable change above that limit.

## APPENDIX B: MAGNETIZATION DYNAMICS

In this section, we describe the model used to simulate the magnetization dynamics. We simplify the model to derive analytical expressions for the switching threshold and the switching time assisted by the exchange coupling. We compare the expressions with the numerical results from the full model assuming magnets with perpendicular anisotropy.

TABLE I. Parameters used for NEGF simulations.

$\Delta_{\text{ex}}$	$\frac{m_f^*}{m_0}$	$\Delta_B$	$\frac{m_{\text{ox}}^*}{m_0}$	$\Delta_{\text{sp}}$	$\frac{m_n^*}{m_0}$	$E_F$	$a$
2.2 eV	1	0.7 eV	0.85	0.4 eV	0.85	2.25 eV	1 Å

Here,  $m_0$  is the free electron mass  $9.1 \times 10^{-31}$  kg.

## 1. LLG equation

We assume single-domain magnets and analyze the magnetization dynamics using a coupled Landau-Lifshitz-Gilbert equation [50,51], given by

$$\begin{aligned} \frac{1 + \alpha_g^2}{\gamma H_{k1}} \frac{d\hat{m}_1}{dt} &= -\hat{m}_1 \times \vec{h}_1 - \alpha_g \hat{m}_1 \times \hat{m}_1 \times \vec{h}_1 \\ &+ \hat{m}_1 \times \frac{\hbar \vec{J}_s S}{4qE_1} \times \hat{m}_1 + \alpha_g \hat{m}_1 \times \frac{\hbar \vec{J}_s S}{4qE_1} \\ &- \hat{m}_1 \times \frac{J_{\text{ex}} S}{E_1} \hat{m}_2 - \alpha_g \hat{m}_1 \times \hat{m}_1 \times \frac{J_{\text{ex}} S}{E_1} \hat{m}_2, \end{aligned} \quad (\text{B1a})$$

$$\begin{aligned} \frac{1 + \alpha_g^2}{\gamma H_{k2}} \frac{d\hat{m}_2}{dt} &= -\hat{m}_2 \times \vec{h}_2 - \alpha_g \hat{m}_2 \times \hat{m}_2 \times \vec{h}_2 \\ &+ \hat{m}_2 \times \frac{\hbar \vec{J}_s S}{4qE_2} \times \hat{m}_2 + \alpha_g \hat{m}_2 \times \frac{\hbar \vec{J}_s S}{4qE_2} \\ &- \hat{m}_2 \times \frac{J_{\text{ex}} S}{E_2} \hat{m}_1 - \alpha_g \hat{m}_2 \times \hat{m}_2 \times \frac{J_{\text{ex}} S}{E_2} \hat{m}_1, \end{aligned} \quad (\text{B1b})$$

where  $\vec{m}_1$  and  $\vec{m}_2$  are the magnetization vectors of the fixed and free layers, respectively,  $S$  is the cross-section area,  $\gamma$  is the gyromagnetic ratio,  $\alpha_g$  is the Gilbert damping constant, and  $E_{1,2}$  are the anisotropy energies of the fixed and the free magnetic layers.  $\vec{J}_s$  is the spin-current density in the structure [given by Eq. (8)]. Note that Eqs. (B1a) and (B1b) are coupled with the exchange coupling energy  $J_{\text{ex}}$  between the magnets [given by Eq. (1)]. Here,  $\vec{h}_{1,2} = \vec{H}_{1,2}/H_{k1,2}$  are the normalized effective magnetic fields with

$$\vec{H}_{1,2} = H_{k1,2} \hat{z} - H_{d1,2} \hat{y} + \vec{H}_{\text{ext}} + \vec{H}_{\text{th}},$$

with  $H_{\text{ext}}$  being the external field.  $H_{k1,2} = 2K_{u,\parallel}/M_{s1,2}$  are the effective anisotropy fields and  $H_{d1,2} = 4\pi N_y M_{s1,2} - 2K_{u,\perp}/M_{s1,2}$  are the demagnetizing fields of the corresponding layers (see, e.g., Ref. [54]). Here,  $K_{u,\parallel}$  and  $K_{u,\perp}$  are in-plane and perpendicular anisotropy constants.

$H_{\text{th}}$  is the random magnetic field to take into account the effect of thermal noise. The random field has zero mean and is totally uncorrelated (see, e.g., Ref. [60]):

$$\langle \vec{H}_{\text{th}} \rangle = 0, \quad (\text{B2a})$$

$$\langle \vec{H}_{\text{th}}(t) H_{\text{th}}(t') \rangle = \frac{\alpha_g}{1 + \alpha_g^2} \frac{2k_B T}{\gamma M_{s2} \Omega_2} \delta(t - t'), \quad (\text{B2b})$$

TABLE II. Parameters used for LLG simulations.

	$M_s$ (emu/cc)	$H_k$ (Oe)	Thickness (nm)	$\alpha_g$
Fixed	1100	300	10	
Free	1100	150	1.5	0.01

Diameter of the device is 150 nm.

where  $\Omega_2$  is the volume of the free layer. The thermal field that enters in Eqs. (B1a) and (B1b) is modeled as [61]

$$|\vec{H}_{\text{th}}| = \sqrt{\frac{\alpha_g}{1 + \alpha_g^2} \frac{2k_B T}{\gamma M_{s2} \Omega_2 \Delta t}} R_{\text{rand}}(t), \quad (\text{B3})$$

where  $R_{\text{rand}}(t)$  is a Gaussian distribute random number. We set  $T = 300$  K and  $\Delta t = 5$  ps for our simulations. We also assume an initial angle of approximately  $5^\circ$  due to thermal fluctuation. The parameters used for simulations are listed in Table II.

## 2. Derivation of switching threshold

In this subsection, we derive an analytical expression for the threshold of switching, assisted only by IEC,  $J_{\text{ex}}$ . So, we turn off the spin current ( $\vec{J}_S = 0$ ), the external magnetic field ( $\vec{H}_{\text{ext}} = 0$ ), and the random field ( $\vec{H}_{\text{th}} = 0$ ), in Eqs. (B1a) and (B1b). For the analytical derivation we assume that the magnets have perpendicular anisotropies (i.e.,  $H_{d1,2} \approx 0$ ). Thus, the  $z$  components of the magnetizations in Eqs. (B1a) and (B1b) reduce to

$$\frac{1 + \alpha_g^2}{\alpha_g \gamma H_{k1}} \frac{dm_{z1}}{dt} = \left( m_{z1} + \frac{J_{\text{ex}} S}{E_1} m_{z2} \right) (1 - m_{z1}^2), \quad (\text{B4a})$$

$$\frac{1 + \alpha_g^2}{\alpha_g \gamma H_{k2}} \frac{dm_{z2}}{dt} = \left( m_{z2} + \frac{J_{\text{ex}} S}{E_2} m_{z1} \right) (1 - m_{z2}^2). \quad (\text{B4b})$$

For parallel conditions:  $m_{z1} = 1 - \delta_1$  and  $m_{z2} = 1 - \delta_2$  or  $m_{z1} = -1 + \delta_1$  and  $m_{z2} = -1 + \delta_2$ , where  $\delta_{1,2} \rightarrow 0$ , we have from Eqs. (B4a) and (B4b)

$$\begin{aligned} -\frac{1 + \alpha_g^2}{\alpha_g \gamma H_{k1}} \frac{d\delta_1}{dt} &\approx 2 \left( 1 + \frac{J_{\text{ex}} S}{E_1} \right) \delta_1, \\ -\frac{1 + \alpha_g^2}{\alpha_g \gamma H_{k2}} \frac{d\delta_2}{dt} &\approx 2 \left( 1 + \frac{J_{\text{ex}} S}{E_2} \right) \delta_2, \end{aligned}$$

which are stable only if

$$(-J_{\text{ex}} \times S) < E_1 \quad \text{and} \quad (-J_{\text{ex}} \times S) < E_2.$$

Similarly, for antiparallel conditions,  $m_{z1} = 1 - \delta_1$  and  $m_{z2} = -1 + \delta_2$  or  $m_{z1} = -1 + \delta_1$  and  $m_{z2} = 1 - \delta_2$ , we

have from Eqs. (B4a) and (B4b)

$$\begin{aligned} -\frac{1 + \alpha_g^2}{\alpha_g \gamma H_{k1}} \frac{d\delta_1}{dt} &\approx 2 \left( 1 - \frac{J_{\text{ex}} S}{E_1} \right) \delta_1, \\ \frac{1 + \alpha_g^2}{\alpha_g \gamma H_{k2}} \frac{d\delta_2}{dt} &\approx 2 \left( -1 + \frac{J_{\text{ex}} S}{E_2} \right) \delta_2, \end{aligned}$$

which are stable only if

$$(J_{\text{ex}} \times S) < E_1 \quad \text{and} \quad (J_{\text{ex}} \times S) < E_2.$$

Thus, the conditions for stability in either parallel or antiparallel configurations are given by

$$\frac{|J_{\text{ex}} S|}{E_1} < 1, \quad (\text{B5a})$$

$$\frac{|J_{\text{ex}} S|}{E_2} < 1, \quad (\text{B5b})$$

which yields the condition for stability as

$$\frac{|J_{\text{ex}} S|}{E_1} + \frac{|J_{\text{ex}} S|}{E_2} < 2. \quad (\text{B6})$$

Thus, the condition required to make any stable configuration unstable is given by

$$\frac{|J_{\text{ex}} S|}{E_1} + \frac{|J_{\text{ex}} S|}{E_2} \geq 2, \quad (\text{B7})$$

which in turn, gives the switching threshold expression in Eq. (5). Note that for simplicity, the expression for switching threshold is derived assuming perpendicular magnetic anisotropy. However, the expression is valid for in-plane magnetic anisotropy as well.

## 3. Switching time

In this subsection, we derive an analytical expression for the switching speed, assisted only by IEC,  $J_{\text{ex}}$ , while  $\vec{J}_S = 0$ ,  $\vec{H}_{\text{ext}} = 0$ , and  $\vec{H}_{\text{th}} = 0$ . We define the switching time as the time taken for the free magnetization to settle down to a magnetization state in order to achieve the minimum energy configuration with respect to the fixed magnet, as dictated by the applied exchange energy. We start from the expressions in Eqs. (B4a) and (B4b), derived from the LLG model [Eqs. (B1a) and (B1b)], under the assumption of perpendicular anisotropy,  $H_{d1,2} \approx 0$ . In addition, for the simplicity of the derivation, we consider comparable anisotropy fields of the two magnets ( $H_{k1} = H_{k2} = H_k$ ). The anisotropy energies of the magnets ( $E_{1,2}$ ) differs by the saturation magnetization and the volume.

We assume that initially the free and the fixed magnets are antiparallel  $m_{z1} = 1 - \delta_1$  and  $m_{z2} = -1 + \delta_2$  and we

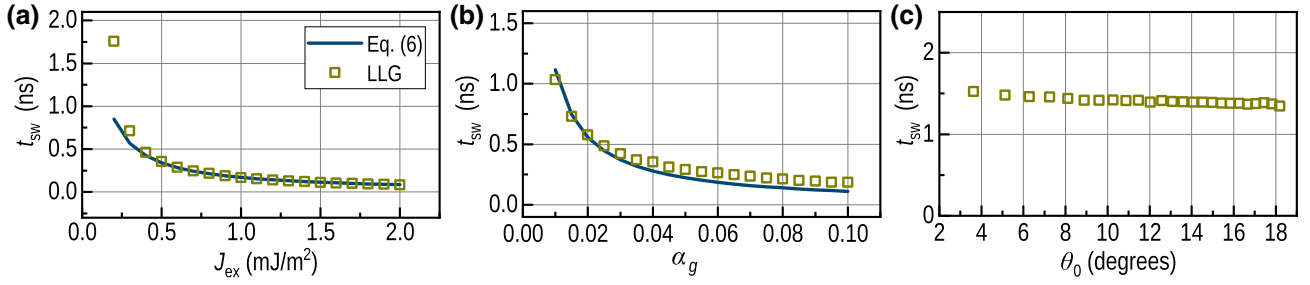


FIG. 9. Comparison of Eq. (6) with numerical simulations using the coupled LLG in Eqs. (B1a) and (B1b). We observe the switching time ( $t_{sw}$ ) as a function of (a) the resonance-enhanced IEC,  $J_{ex}$ , (b) the Gilbert damping,  $\alpha_g$ , and (c) initial angle of the free magnet,  $\theta_0$ .

set  $J_{ex} < 0$  to make this configuration unstable. Thus, from Eq. (B4b) we get

$$\frac{1 + \alpha_g^2}{\alpha_g \gamma H_k} \frac{d\delta_2}{dt} \approx -2 \left( 1 + \frac{|J_{ex}|S}{E_2} \right) \delta_2, \quad (\text{B8})$$

and the characteristic  $\tau_2$  time is given by

$$\frac{1}{\tau_2} = \frac{2\alpha_g \gamma H_k}{1 + \alpha_g^2} \left( 1 + \frac{|J_{ex}|S}{E_2} \right). \quad (\text{B9})$$

Similarly, from Eq. (B4a) we get

$$-\frac{1 + \alpha_g^2}{\alpha_g \gamma H_k} \frac{d\delta_1}{dt} \approx -2 \left( -1 + \frac{|J_{ex}|S}{E_1} \right) \delta_1, \quad (\text{B10})$$

and the characteristic time  $\tau_1$  is given by

$$\frac{1}{\tau_1} = \frac{2\alpha_g \gamma H_k}{1 + \alpha_g^2} \left( -1 + \frac{|J_{ex}|S}{E_1} \right). \quad (\text{B11})$$

Since, we assume that the free magnet settles down to a parallel configuration (required by  $J_{ex} < 0$ ) starting from an antiparallel configuration, there is a sign difference in the rate of change in Eqs. (B8) and (B10). The total characteristic time to settle down from one magnetic state to the other due to a sign change in  $J_{ex}$  is given by

$$\frac{1}{t_{sw}} = \frac{1}{\tau_1} + \frac{1}{\tau_2} = \frac{2\alpha_g \gamma H_k}{1 + \alpha_g^2} \left( \frac{|J_{ex}|S}{E_1} + \frac{|J_{ex}|S}{E_2} \right),$$

which yields the expression in Eq. (6), as given by

$$t_{sw} = \frac{1 + \alpha_g^2}{4\alpha_g \gamma H_k} \frac{J_{ex0}}{|J_{ex}|},$$

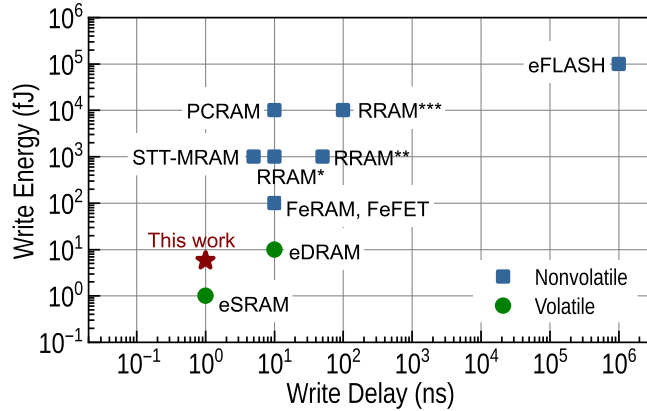


FIG. 10. Comparison of write energy and delay of this work with existing memory technologies [15]: embedded static random access memory (eSRAM), embedded dynamic random access memory (eDRAM), ferroelectric random access memory and field-effect transistor (FeRAM, FeFET), resistive random access memory (RRAM), spin-transfer-torque random access memory (STT MRAM), phase-change random access memory (PCRAM), and embedded FLASH memory (eFLASH). \*\*crossbar-RRAM. \*\*\*vertical-RRAM.

where  $J_{ex0}$  is the switching threshold give by Eq. (5).

We compare Eq. (6) with numerical simulations using the full LLG model in Eqs. (B1a) and (B1b) assuming perpendicular anisotropies and comparable  $H_k$ , as shown in Fig. 9. In the simulations, magnets are antiparallel initially. We change the sign of  $J_{ex}$  at  $t = t_1$  and calculate the time  $t_2$  at which the free magnetization is 90% of its expected final value. We define the numerical switching time  $t_{sw} = t_2 - t_1$ . We observe that the switching time from LLG simulations scales inversely with both the Gilbert damping and the applied exchange coupling strength [see Figs. 9(a)–(b)], in agreement with Eq. (6). The dependence of the numerical  $t_{sw}$  on the initial angle is negligible as shown in Fig. 9(c).

#### 4. Switching energy and delay

The write energy and delay are important figure of merits for memory applications. For the device discussed here, we calculate the write delay and speed of our free magnet with in-plane anisotropy using the coupled LLG equations in Eqs. (B1a) and (B1b). The switching speed of the

device is  $\tau \approx 1$  ns (see Fig. 3). The switching voltages to have ferromagnetic and antiferromagnetic configurations are  $V_{\text{in}} = 1.3$  V and 1.6 V, respectively. The current density in the structure is approximately  $10^4$  A/cm<sup>2</sup> at 1.6 V [see Fig. 6(a)]. For a device with a diameter of 150 nm, the current flowing in the structure is  $I \approx 1.8$   $\mu$ A, which corresponds to a structure resistance of  $R \approx 889$  k $\Omega$ . The power consumed by a write operation to an antiferromagnetic configuration is calculated as  $P = I^2 R \approx 2.88$   $\mu$ W. If we apply a voltage pulse of width  $2\tau$ , the energy consumed during the write operation is  $2P\tau \approx 5.76$  fJ. We compare the estimated switching energy and delay of this work with various existing memory technologies, as shown in Fig. 10: embedded static random access memory (eSRAM), embedded dynamic random access memory (eDRAM), ferroelectric random access memory and field-effect transistor (FeRAM, FeFET), resistive random access memory (RRAM), spin-transfer-torque random access memory (STT MRAM), phase-change random access memory (PCRAM), and embedded FLASH memory (eFLASH). The data used for the comparison are taken from Ref. [15]. The estimated delay is similar to that observed in eSRAM, and the estimated energy is lower than that observed in eDRAM.

### APPENDIX C: CONSERVATIVE AND NONCONSERVATIVE TORQUES

In this appendix, we discuss the nature of the torques applied by the spin current and the interlayer exchange coupling.

As mentioned in Eq. (7) that  $G^n$  in Eq. (A13) can be written as

$$G^n = A \frac{f_1 + f_2}{2} + (A_1 - A_2) \frac{f_1 - f_2}{2}.$$

According to Eqs. (1) and (2), the IEC energy depends on  $\vec{\sigma} G^n$ . We have an equilibrium value of IEC (i.e.,  $f_1 = f_2$ ) due to the first term in Eq. (7), given that the transmission coefficient between the two magnets is sufficiently high. That term corresponds to occupied electronic states, which in turn, determines the strength of the IEC. However, the spin-torque devices largely rely on the second term in Eq. (7), determined by the  $A_1 - A_2$  and proportional to the current flowing in the structure.

Individually  $A_{1,2}$  are Hermitian but not symmetric, but  $A = A_1 + A_2 = i(G^R - G^A)$  is symmetric.

$$A_{1,2}^T \neq A_{1,2} \quad \text{and} \quad A^T = A.$$

This means that  $A$  is purely real and we can express  $A$  and  $A_1 - A_2$  as

$$A = P\sigma_z + Q\sigma_x, \quad (\text{C1a})$$

$$A_1 - A_2 = P'\sigma_z + Q'\sigma_x + R'\sigma_y. \quad (\text{C1b})$$

The torque determined by  $A$  can be expressed as

$$\vec{\tau} = \vec{m}_1 \times (a\vec{m}_1 + b\vec{m}_2) = \vec{m}_1 \times b\vec{m}_2. \quad (\text{C2})$$

Here,  $b\vec{m}_2$  is the applied force on the free magnetization  $\vec{m}_1$ . On the other hand,  $A_1 - A_2$  component has an additional component along  $\vec{m}_1 \times \vec{m}_2$ , given by

$$\begin{aligned} \vec{\tau} &= \vec{m}_1 \times [a'\vec{m}_1 + b'\vec{m}_2 + c'(\vec{m}_1 \times \vec{m}_2)] \\ &= \vec{m}_1 \times [b'\vec{m}_2 + c'(\vec{m}_1 \times \vec{m}_2)], \end{aligned} \quad (\text{C3})$$

where  $\vec{F} = b'\vec{m}_2 + c'(\vec{m}_1 \times \vec{m}_2)$  is the applied force on the free magnetization  $\vec{m}_1$ .

For simplicity, we assume  $\vec{m}_1$  is along  $\hat{z}$  direction and  $\vec{m}_2$  is defined in a spherical co-ordinate system, hence, we can write

$$\vec{F} = F_m \hat{m} + F_\phi \hat{\phi} + F_\theta \hat{\theta}, \quad (\text{C4})$$

with

$$\begin{aligned} \hat{m} &\equiv (\sin \theta \cos \phi, \sin \theta \sin \phi, \cos \theta), \\ \hat{\theta} &\equiv (\cos \theta \cos \phi, \cos \theta \sin \phi, -\sin \theta), \\ \hat{\phi} &\equiv (-\sin \phi, \cos \phi, 0). \end{aligned}$$

Here,  $\hat{\phi}$  direction is the out-of-plane direction given by  $\vec{m}_1 \times \vec{m}_2$  in Eq. (C3).

We assume  $|\vec{m}| = 1$  and  $\phi = 0$  and write the curl of  $\vec{F}$  as

$$\vec{\nabla}_m \times \vec{F} = \frac{\hat{m}}{\sin \theta} \frac{\partial}{\partial \theta} (\sin \theta F_\phi) - \hat{\phi} \frac{\partial}{\partial \theta} F_m. \quad (\text{C5})$$

Note that the component along  $\hat{m}$  do not contribute to total torque and hence we can assume  $F_m$  to be arbitrarily constant. Thus Eq. (C5) becomes

$$\vec{\nabla}_m \times \vec{F} = \frac{\hat{m}}{\sin \theta} \frac{\partial}{\partial \theta} (\sin \theta F_\phi), \quad (\text{C6})$$

which is nonzero indicating that  $\vec{F}$  is nonconservative due to the out-of-plane component  $F_\phi$ , which occurs due to the second component in Eq. (7). It is easy to see that first term in Eq. (7) corresponds to a conservative torque.

- 
- [1] L. Berger, Emission of spin waves by a magnetic multilayer traversed by a current, *Phys. Rev. B* **54**, 9353 (1996).
  - [2] J. C. Slonczewski, Current-driven excitation of magnetic multilayers, *J. Magn. Magn. Mater* **159**, L1 (1996).



- [3] I. M. Miron, K. Garello, G. Gaudin, P.-J. Zermatten, M. V. Costache, S. Auffret, S. Bandiera, B. Rodmacq, A. Schuhl, and P. Gambardella, Perpendicular switching of a single ferromagnetic layer induced by in-plane current injection, *Nature* **476**, 189 (2011).
- [4] T. Suzuki, S. Fukami, N. Ishiwata, M. Yamanouchi, S. Ikeda, N. Kasai, and H. Ohno, Current-induced effective field in perpendicularly magnetized Ta/CoFeB/MgO wire, *Appl. Phys. Lett.* **98**, 142505 (2011).
- [5] L. Liu, C.-F. Pai, Y. Li, H. W. Tseng, D. C. Ralph, and R. A. Buhrman, Spin-torque switching with the giant spin Hall effect of tantalum, *Science* **336**, 555 (2012).
- [6] C. Chappert, A. Fert, and F. N. Van Dau, The emergence of spin electronics in data storage, *Nat. Mater.* **6**, 813 (2007).
- [7] D. Apalkov, B. Dieny, and J. M. Slaughter, Magnetoresistive random access memory, *Proc. IEEE* **104**, 1796 (2016).
- [8] G. Prenat, K. Jabeur, G. D. Pendina, O. Boulle, and G. Gaudin, *Beyond STT-MRAM, Spin Orbit Torque ram SOT-MRAM for High Speed and High Reliability Applications, Spintronics-Based Computing* (Springer International Publishing, Switzerland, 2015).
- [9] S. Sayed, S. Hong, E. E. Marinero, and S. Datta, Proposal of a single nano-magnet memory device, *IEEE Electron Device Lett.* **38**, 1665 (2017).
- [10] F. Matsukura, Y. Tokura, and H. Ohno, Control of magnetism by electric fields, *Nat. Nanotechnol.* **10**, 209 (2015).
- [11] T. Newhouse-Illige, Y. Liu, M. Xu, D. Reifsnnyder Hickey, A. Kundu, H. Almasi, C. Bi, X. Wang, J. W. Freeland, D. J. Keavney, C. J. Sun, Y. H. Xu, M. Rosales, X. M. Cheng, S. Zhang, K. A. Mkhoyan, and W. G. Wang, Voltage-controlled interlayer coupling in perpendicularly magnetized magnetic tunnel junctions, *Nat. Commun.* **8**, 15232 (2017).
- [12] L. Wang, W. Kang, F. Ebrahimi, X. Li, Y. Huang, C. Zhao, K. L. Wang, and Weisheng Zhao, Voltage-controlled magnetic tunnel junctions for processing-in-memory implementation, *IEEE Electron Device Lett.* **39**, 440 (2018).
- [13] R. O. Cherifi, V. Ivanovskaya, L. C. Phillips, A. Zobelli, I. C. Infante, E. Jacquet, V. Garcia, S. Fusil, P. R. Briddon, N. Guiblin, A. Mougin, A. A. Ünal, F. Kronast, S. Valencia, B. Dkhil, A. Barthélemy, and M. Bibes, Electric-field control of magnetic order above room temperature, *Nat. Mater.* **13**, 345 (2014).
- [14] J. T. Heron, J. L. Bosse, Q. He, Y. Gao, M. Trassin, L. Ye, J. D. Clarkson, C. Wang, Jian Liu, S. Salahuddin, D. C. Ralph, D. G. Schlom, J. Íñiguez, B. D. Huey, and R. Ramesh, Deterministic switching of ferromagnetism at room temperature using an electric field, *Nature* **516**, 370 (2014).
- [15] S. Salahuddin, K. Ni, and S. Datta, The era of hyper-scaling in electronics, *Nat. Electron.* **1**, 442 (2018).
- [16] C.-Y. You and S. D. Bader, Prediction of switching/rotation of the magnetization direction with applied voltage in a controllable interlayer exchange coupled system, *J. Magn. Mater.* **195**, 488 (1999).
- [17] X. Fan, G. Wei, X. Lin, X. Wang, Z. Si, X. Zhang, Q. Shao, S. Mangin, E. Fullerton, L. Jiang, and W. Zhao, Reversible switching of interlayer exchange coupling through atomically thin VO<sub>2</sub> via electronic state modulation, *Matter* **2**, 1582 (2020).
- [18] C. Bi, Y. Liu, T. Newhouse-Illige, M. Xu, M. Rosales, J. W. Freeland, O. Mryasov, S. Zhang, S. G. E. te Velthuis, and W. G. Wang, Reversible Control of Co Magnetism by Voltage-Induced Oxidation, *Phys. Rev. Lett.* **113**, 267202 (2014).
- [19] U. Bauer, L. Yao, A. J. Tan, P. Agrawal, S. Emori, H. L. Tuller, S. van Dijken, and G. S. D. Beach, Magneto-ionic control of interfacial magnetism, *Nat. Mater.* **14**, 174 (2014).
- [20] Q. Yang, L. Wang, Z. Zhou, L. Wang, Y. Zhang, S. Zhao, G. Dong, Y. Cheng, T. Min, Z. Hu, W. Chen, K. Xia, and M. Liu, Ionic liquid gating control of RKKY interaction in FeCoB/Ru/FeCoB and (Pt/Co)<sub>2</sub>/Ru/(Co/Pt)<sub>2</sub> multilayers, *Nat. Commun.* **9**, 991 (2018).
- [21] D. Zhang, M. Bapna, W. Jiang, D. P. de Sousa, Y.-C. Liao, Z. Zhao, Y. Lv, A. Naemi, T. Low, S. A. Majetich, and J.-P. Wang, Bipolar electric-field switching of perpendicular magnetic tunnel junctions through voltage-controlled exchange coupling, arXiv:1912.10289 [physics.app-ph] (2019).
- [22] R. S. Liu, S.-H. Yang, X. Jiang, X.-G. Zhang, C. Rettner, L. Gao, T. Topuria, P. M. Rice, W. Zhang, C. M. Canali, and S. S. P. Parkin, CoFe alloy as middle layer for strong spin dependent quantum well resonant tunneling in MgO double barrier magnetic tunnel junctions, *Phys. Rev. B* **87**, 024411 (2013).
- [23] B. S. Tao, H. X. Yang, Y. L. Zuo, X. Devaux, G. Lengaigne, M. Hehn, D. Lacour, S. Andrieu, M. Chshiev, T. Hauet, F. Montaigne, S. Mangin, X. F. Han, and Y. Lu, Long-Range Phase Coherence in Double-Barrier Magnetic Tunnel Junctions with a Large Thick Metallic Quantum Well, *Phys. Rev. Lett.* **115**, 157204 (2015).
- [24] Z. Y. Liu and S. Adenwalla, Oscillatory Interlayer Exchange Coupling and its Temperature Dependence in Pt/Co<sub>3</sub>/NiO/Co/Pt<sub>3</sub> Multilayers with Perpendicular Anisotropy, *Phys. Rev. Lett.* **91**, 037207 (2003).
- [25] H. Yang, S.-H. Yang, D.-C. Qi, A. Rusydi, H. Kawai, M. Saeys, T. Leo, D. J. Smith, and S. S. P. Parkin, Negative Tunneling Magnetoresistance by Canted Magnetization in MgO/NiO Tunnel Barriers, *Phys. Rev. Lett.* **106**, 167201 (2011).
- [26] S. Yuasa, T. Nagahama, and Y. Suzuki, Spin-polarized resonant tunneling in magnetic tunnel junctions, *Science* **297**, 234 (2002).
- [27] S. S. P. Parkin, Systematic Variation of the Strength and Oscillation Period of Indirect Magnetic Exchange Coupling through the 3 d, 4 d, and 5 d Transition Metals, *Phys. Rev. Lett.* **67**, 3598 (1991).
- [28] F. Petroff, A. Barthélemy, D. H. Mosca, D. K. Lottis, A. Fert, P. A. Schroeder, W. P. Pratt, R. Loloee, and S. Lequien, Oscillatory interlayer exchange and magnetoresistance in Fe/Cu multilayers, *Phys. Rev. B* **44**, 5355 (1991).
- [29] E. E. Fullerton, M. J. Conover, J. E. Mattson, C. H. Sowers, and S. D. Bader, Oscillatory interlayer coupling and giant magnetoresistance in epitaxial Fe/Cr(211) and (100) superlattices, *Phys. Rev. B* **48**, 15755 (1993).
- [30] W. R. Bennett, W. Schwarzscher, and W. F. Egelhoff, Concurrent Enhancement of Kerr Rotation and Antiferromagnetic Coupling in Epitaxial Fe/Cu/Fe Structures, *Phys. Rev. Lett.* **65**, 3169 (1990).

- [31] S. Toscano, B. Briner, H. Hopster, and M. Landolt, Exchange-coupling between ferromagnets through a non-metallic amorphous spacer-layer, *J. Magn. Magn. Mater* **114**, L6 (1992).
- [32] J. C. Slonczewski, Overview of interlayer exchange theory, *J. Magn. Magn. Mater* **150**, 13 (1995).
- [33] P. Bruno, Theory of interlayer magnetic coupling, *Phys. Rev. B* **52**, 411 (1995).
- [34] P. M. Haney, C. Heiliger, and M. D. Stiles, Bias dependence of magnetic exchange interactions: Application to interlayer exchange coupling in spin valves, *Phys. Rev. B* **79**, 054405 (2009).
- [35] J. Mathon, M. Villeret, D. M. Edwards, and R. B. Muniz, Theory of oscillatory exchange in magnetic multilayers: Effect of partial confinement and band mismatch, *J. Magn. Magn. Mater* **121**, 242 (1993).
- [36] Y. F. Chiang, Jared J. I. Wong, X. Tan, Yan Li, K. Pi, W. H. Wang, H. W. K. Tom, and R. K. Kawakami, Oxidation-induced biquadratic coupling in Co/Fe/MgO/Fe(001), *Phys. Rev. B* **79**, 184410 (2009).
- [37] J. Faure-Vincent, C. Tiusan, C. Bellouard, E. Popova, M. Hehn, F. Montaigne, and A. Schuhl, Interlayer Magnetic Coupling Interactions of Two Ferromagnetic Layers by Spin Polarized Tunneling, *Phys. Rev. Lett.* **89**, 107206 (2002).
- [38] L. L. Chang, L. Esaki, and R. Tsu, Resonant tunneling in semiconductor double barriers, *Appl. Phys. Lett.* **24**, 593 (1974).
- [39] R. Suzuki, Y. K. Wakabayashi, K. Okamoto, M. Tanaka, and S. Ohya, Quantum size effect in an Fe quantum well detected by resonant tunneling carriers injected from a *p*-type Ge semiconductor electrode, *Appl. Phys. Lett.* **112**, 152402 (2018).
- [40] Nonreciprocal spin pumping damping in asymmetric magnetic trilayers.
- [41] K. Yakushiji, A. Sugihara, A. Fukushima, H. Kubota, and S. Yuasa, Very strong antiferromagnetic interlayer exchange coupling with iridium spacer layer for perpendicular magnetic tunnel junctions, *Appl. Phys. Lett.* **110**, 092406 (2017).
- [42] A. Dinia, S. Zoll, M. Gester, D. Stoeffler, J. P. Jay, K. Ounadjela, H. A. M. van den Berg, and H. Rakoto, Interfacial polarisation effect on the interlayer couplings in Co/Rh sandwiches, *Eur. Phys. J. B* **5**, 203 (1998).
- [43] F. Schleicher *et al.*, Localized states in advanced dielectrics from the vantage of spin- and symmetry-polarized tunnelling across MgO, *Nat. Commun.* **5**, 4547 (2014).
- [44] S. Yuasa, T. Nagahama, A. Fukushima, Y. Suzuki, and K. Ando, Giant room-temperature magnetoresistance in single-crystal Fe/MgO/Fe magnetic tunnel junctions, *Nat. Mater.* **3**, 868 (2004).
- [45] H. Kubota, A. Fukushima, K. Yakushiji, T. Nagahama, S. Yuasa, K. Ando, H. Maehara, Y. Nagamine, K. Tsunekawa, D. D. Djayaprawira, N. Watanabe, and Y. Suzuki, Quantitative measurement of voltage dependence of spin-transfer torque in MgO-based magnetic tunnel junctions, *Nat. Phys.* **4**, 37 (2008).
- [46] D. Datta, B. Behin-Aein, S. Datta, and S. Salahuddin, Voltage asymmetry of spin-transfer torques, *IEEE Trans. Nanotechnol.* **11**, 261 (2012).
- [47] I. Bar-Joseph, Y. Gedalyahu, A. Yacoby, T. K. Woodward, D. S. Chemla, D. L. Sivco, and A. Y. Cho, Temperature dependence of the resonant-tunneling process in a double-barrier diode, *Phys. Rev. B* **44**, 8361 (1991).
- [48] S. Schwieger, J. Kienert, K. Lenz, J. Lindner, K. Baberschke, and W. Nolting, Temperature dependence of interlayer exchange coupling, *J. Magn. Magn. Mater* **310**, 2301 (2007).
- [49] Y. Li, X. Jin, P. Pan, F. N. Tan, W. S. Lew, and F. Ma, Temperature-dependent interlayer exchange coupling strength in synthetic antiferromagnetic [Pt/Co]<sub>2</sub>/Ru/[Co/Pt]<sub>4</sub> multilayers, *Chin. Phys. B* **27**, 127502 (2018).
- [50] R. H. Victora and X. Shen, Composite media for perpendicular magnetic recording, *IEEE Trans. Magn* **41**, 537 (2005).
- [51] K. Y. Camsari, A. Z. Pervaiz, R. Faria, E. E. Marinero, and S. Datta, Ultrafast spin-transfer-Torque switching of synthetic ferrimagnets, *IEEE Magn. Lett.* **7**, 1 (2016).
- [52] J. Z. Sun, Spin-current interaction with a monodomain magnetic body: A model study, *Phys. Rev. B* **62**, 570 (2000).
- [53] S. Salahuddin, D. Datta, and S. Datta, Spin Transfer Torque as a Non-Conservative Pseudo-Field, arXiv:0811.3472 [cond-mat.mes-hall] (2008).
- [54] A. Sharma, A. A. Tulapurkar, and B. Muralidharan, Resonant Spin-Transfer-Torque Nano-Oscillators, *Phys. Rev. Appl.* **8**, 064014 (2017).
- [55] A. G. Petukhov, A. N. Chantis, and D. O. Demchenko, Resonant Enhancement of Tunneling Magnetoresistance in Double-Barrier Magnetic Heterostructures, *Phys. Rev. Lett.* **89**, 107205 (2002).
- [56] C. H. Chen and W. J. Hsueh, Enhancement of tunnel magnetoresistance in magnetic tunnel junction by a superlattice barrier, *Appl. Phys. Lett.* **104**, 042405 (2014).
- [57] A. Sharma, A. A. Tulapurkar, and B. Muralidharan, Band-pass fabry-pèrot magnetic tunnel junctions, *Appl. Phys. Lett.* **112**, 192404 (2018).
- [58] R. Rios, A. A. Sharma, V. H. Le, G. W. Dewey, and J. T. Kavalieros, Two transistor, one resistor non-volatile gain cell memory and storage element, US Patent App. 16/320, 023 (2019).
- [59] S. Datta, *Electronic Transport in Mesoscopic Systems* (Cambridge University Press, Cambridge, 1995), p. 377.
- [60] B. Behin-Aein, D. Datta, S. Salahuddin, and S. Datta, Proposal for an all-spinlogic device with built-in memory, *Nat. Nanotechnol.* **5**, 266 (2010).
- [61] J.-G. Zhu, Thermal magnetic noise and spectra in spin valve heads, *J. Appl. Phys.* **91**, 7273 (2002).